Ore Geology Reviews 104 (2019) 356–372

Contents lists available at ScienceDirect

Ore Geology Reviews

journal homepage: www.elsevier.com/locate/oregeorev

Formation of the Lubei magmatic Ni–Cu deposit in a post-subduction setting in East Tianshan, North West China

Baoyun Chen[a], Jinjie Yu[a,*], Shuaijie Liu[a,b], Jiangtao Tian[c]

[a] MNR Key Laboratory of Metallogeny and Mineral Assessment, Institute of Mineral Resources, CAGS, Beijing 100037, China
[b] Department of Earth and Space Sciences, Southern University of Science and Technology, Shenzhen 518055, Guangdong Province, China
[c] Xinjiang Geological Survey, Urumqi 830000, Xinjiang, China

ARTICLE INFO

Keywords:
Lubei Ni–Cu deposit
Partial mantle melting
Sulfide segregation
Platinum group element
Post-subduction setting
North Xinjiang

ABSTRACT

The Lubei Ni–Cu sulfide ore deposit with 7.8 Mt sulfide ores at an average grade of 0.88 wt% Ni and 0.5 wt% Cu, is associated with a mafic–ultramafic intrusion in the western part of the East Tianshan in Xinjiang Uygur Autonomous Region, NW China. The primary mineralization is hosted by ultramafic rocks which are part of a 2.1 km^2 mafic–ultramafic intrusion located within the Kanggurtag fault zone. In this paper, we intend to probe the ore-formation processes for the Lubei Ni–Cu sulfide ore deposit and discuss key factors that control the ore formation processes in a post-subduction setting. The Lubei primary magmas were derived from 13 to 17 % partial melting of a hydrous mantle containing ~0.29 wt% H_2O estimated using the silicate-liquid model pMELTS. The Lubei sulfide ores are characterized by low platinum group elements (PGE) and high mantle-normalized Pd/Ir ratios, and disseminated sulfide ores have higher Cu, Ni and PGE tenors than massive and vein sulfide ores indicative of crystal fractionation of Fe-rich monosulfide solid solution. The PGE-depleted Lubei sulfides possibly resulted from early sulfide segregation from the Lubei primary magmas as indicated by high Cu/Pd ratios (up to 10^6), and the proportion of early sulfide losses was 0.02 wt% which has depleted the Lubei parental magmas and later fractionated sulfides in chalcophile elements. This depletion would been compensated at different levels by later sulfide–magma interaction when the parental magmas reached *in situ* sulfide saturation, with an R factor (mass ratio of silicate to sulfide liquids) of 100–1000. The formation of the observed Lubei disseminated sulfide ores was associated with 5–15 vol% magma crystallization with the main silicate minerals being spinel and olivine, as modeled using the silicate-liquid model MELTS. The $\delta^{34}S$ values of the Lubei sulfides vary over a narrow range of −0.3 to +1.8‰, indicating a mantle origin for the sulfur. The key factor that controls the formation of magmatic Ni–Cu deposits in post-subduction settings is a metasomatized mantle accompanied by activation of translithospheric faults during post-collisional extension. This mechanism alternatively interprets the widespread magmatic Ni–Cu deposits in the southern Central Asian Orogenic Belt and implies translithospheric fault as a potential target for Ni–Cu exploration.

1. Introduction

Many of the world's great magmatic Ni–Cu ± platinum group element (PGE) deposits, like Noril'sk and Pechenga (Russia), Thompson and Voisey's Bay (Canada), Jinchuan (China), and the Duluth Complex (USA), appear to occur in extensional plate tectonic settings (Naldrett 2004). Recently, it is recognized that convergent tectonic settings, such as subduction-related magmatic arcs, can also host significant magmatic Ni–Cu ± PGE deposits (Sappin et al., 2011); e.g., Aguablanca (Spain) (Casquet et al. 2001) and Portneuf–Mauricie Domain (PMD, Canada) Ni–Cu sulfide prospects (Sappin et al., 2011), and Xiarihamu (West China) giant Ni–Cu deposit (Li et al., 2015; Song et al., 2016; Zhang et al., 2017). Most Ni–Cu sulfide ore deposits in the southern Central Asian Orogenic Belt (CAOB) are hosted in Early Permian mafic–ultramafic intrusions such as the Kalatongke (Song and Li, 2009) and Poyi (Xia et al., 2013) deposits, and the Huangshan-Jing'erquan Ni–Cu ore belt (Mao et al., 2008) in North Xinjiang, NW China, and in Triassic mafic–ultramafic intrusions such as the Hongqiling deposit in Jilin province, NE China (Wei et al., 2013). These host intrusions occurred in post-subduction tectonic settings accompanied by Early Permian to Triassic post-collisional extension (Xiao et al., 2004; Xiao et al., 2009; Song and Li, 2009; Song et al., 2011; Wei et al., 2013; Chen et al., 2018), and are associated with major translithospheric strike-slip structures (Lightfoot and Evans-Lamswood, 2015).

* Corresponding author.
E-mail address: yjjchina@sina.com (J. Yu).

https://doi.org/10.1016/j.oregeorev.2018.11.017
Received 22 June 2018; Received in revised form 8 November 2018; Accepted 17 November 2018
Available online 20 November 2018

It has long been documented that most magmatic Ni–Cu deposits in the southern CAOB are depleted in platinum group element (PGE) with high Cu/Pd ratios, such as the Kalatongke deposit (Song and Li, 2009) and the Huangshan Jing'erquan Ni–Cu ore belt in North Xinjiang (Mao et al., 2008) and the Hongqiling deposit in Jilin province (Wei et al., 2013). This depletion in PGE was generally attributed to early sulfide segregation (Song and Li, 2009; Tang et al., 2011; Wei et al., 2013; Deng et al., 2014; Zhao et al., 2015a,b; Mao et al., 2014, 2015). Degree of partial mantle melting is a significant factor that controls the Cu, Ni and PGE contents of sulfide ores (Keays, 1995; Barnes and Lightfoot, 2005; Song et al., 2009; Lightfoot et al., 2012), but its influence on the PGE characteristics of the Ni–Cu sulfide ore deposits in the southern CAOB is unclear.

The Lubei Ni–Cu sulfide ore deposit, containing 7.8 Mt sulfide ores at an average grade of 0.88 wt% Ni and 0.5 wt% Cu, is located in the western part of the East Tianshan region (Xinjiang Geological Survey, 2014) and forms the western extension of the Huangshan–Jing'erquan Ni–Cu ore belt (Chen et al., 2018), which contains > 50 Mt sulfide ores at an average grade of 0.52 wt% Ni and 0.27 wt% Cu (Wang et al., 1987; Mao et al., 2015). The Lubei mafic–ultramafic intrusion was derived from a metasomatized mantle previously modified by slab-derived hydrous fluids and formed in a post-subduction setting accompanied by post-collisional extension (Chen et al., 2018). The Lubei Ni–Cu sulfide ore deposit reveals a high Ni–Cu potential for the western part of the East Tianshan, which lacks exploration work until the discovery of the Lubei Ni–Cu sulfide ore deposit in 2014. It is thus important to probe the ore-formation processes and discuss the Ni–Cu exploration potential in a post-subduction setting. In this paper, (1) we model the degree of partial mantle melting using the silicate-liquid model pMELTS and the primary magma compositions calculated by Chen et al. (2018), (2) present sulfur isotopes and PGE geochemistry of the Lubei sulfide ores and model early sulfide segregation and later sulfide–magma interaction during magma evolution, (3) establish the relationship between magma crystallization and sulfide saturation using the silicate-liquid model MELTS and the forsterite (Fo) and Ni contents of olivine, and (4) discuss the key factors that control the formation of a magmatic Ni–Cu deposit in post-subduction settings accompanied by post-collisional extension and present implications for Ni–Cu exploration.

2. Regional geological setting

The North Xinjiang region is located on the southern margin of the CAOB which is bounded by the Siberian Craton to the north and the North China–Tarim Craton to the south and extends E–W for more than 7000 km (Fig. 1a) (Sengör et al., 1993). The tectonic framework of the North Xinjiang region comprises, from north to south, the Chinese Altai, Junggar, and Tianshan domains, and the Paleozoic Beishan rift (Fig. 1b). Numerous Early Permian sulfide-bearing mafic–ultramafic intrusions occur along translithospheric faults which bound different tectonic units in North Xinjiang (Fig. 1b; Mao et al., 2008; Lightfoot and Evans-Lamswood, 2015). The east–west-trending Tianshan domain includes the Northern, Central, and Southern Tianshan terranes (Fig. 1b) (Rui et al., 2002). The so-called Chinese East Tianshan, the eastern sector of the Tianshan domain, comprises the Jueluotage belt (Northern Tianshan) and Central Tianshan massif, separated by the Arqikekuduke–Shaquanzi Fault (Fig. 1c; Xiao et al., 2004; Qin et al., 2011). The Jueluotage belt comprises Carboniferous calc-alkaline volcanic and sedimentary rocks (Pirajno et al., 2011) and is subdivided, from north to south, into the Dananhu–Tousuquan island arc terrane, Wutongwozi–Xiaorequanzi intra-arc basin, Kanggurtag intra-arc basin, and Aqishan–Yamansu arc terrane (Fig. 1c; Xiao et al., 2004; Su et al., 2011). The Central Tianshan massif comprises mainly volcaniclastic rocks and late Proterozoic basement inliers (Pirajno et al., 2011).

Most Permian mafic–ultramafic intrusions are concentrated in the eastern part of the Jueluotage belt, forming the Huangshan–Jing'erquan intrusive belt (Ni–Cu ore belt) (Fig. 1c; Mao et al., 2008). In its western counterpart, there are more than 20 newly discovered mafic–ultramafic intrusions that outcrop in the Qiatekaer region, extending E–W alongside the Kanggurtag Fault in an area of about 50 km E–W by 10 km N–S (Fig. 1c). These mafic–ultramafic intrusions comprise ~70 vol% gabbro, hornblende gabbro, gabbronorite, olivine gabbro, and ~30 vol % ultramafic units (Yang et al., 2017; Chen et al., 2018). No economic Ni–Cu orebodies have been identified except for those hosted in the Lubei mafic–ultramafic intrusion in the westernmost part of the Qiatekaer region (Fig. 1c).

3. Geology, petrology and mineralization of the Lubei intrusion

3.1. Geology

The Lubei mafic–ultramafic intrusion has been fully described by Chen et al. (2018), and details are summarized here. The intrusion has a surface area of ~2.1 km^2, comprising ultramafic rocks in its southern part, gabbro in the central part, and hornblende gabbro in its northern part (Fig. 2). The southern ultramafic sub-intrusion is ~0.6 km^2 and has an elliptical morphology at the surface with its long axis striking E–W. It comprises mainly hornblende peridotite, lherzolite, and harzburgite from top to bottom in the A–B and C–D cross-sections and forms a layered intrusion dipping to the south (Fig. 3). The top hornblende peridotite has sharp contacts with the underlying lherzolite in terms of both field observations and mineral compositions while the lherzolite and harzburgite has gradational contacts (Chen et al., 2018). The northern hornblende gabbro sub-intrusion is ~1.1 km^2 and has an elongated rhomboid shape with an aspect ratio of 1:5. This sub-intrusion is homogeneously composed of hornblende gabbro (Fig. 2). The middle gabbro sub-intrusion is ~0.4 km^2 and has an irregular morphology (Fig. 2). Diorite also outcrops in the eastern part of the Lubei district, with a similar lithology to the intermediate intrusive rocks that are widely distributed in the Qiatekaer region (Xinjiang Geological Survey, 2014). Both the Lubei mafic–ultramafic intrusion and the diorite intrude Lower Carboniferous pyroclastic and clastic rocks in the Lubei district (Fig. 2).

3.2. Petrology

The petrology was reported by Chen et al. (2018), and details are summarized here. The Lubei intrusion has been divided into three formation phases on the basis of location, lithology, and emplacement history. Phase I includes gabbro and hornblende gabbro in the middle and northern parts with lherzolite and harzburgite of phase II, and hornblende peridotite of phase III in the southern part (Figs. 2 and 3).

Phase I: Hornblende gabbro has a cumulate texture and is mainly composed of plagioclase (> 70 vol%) and hornblende with accessory quartz, magnetite, apatite and ilmenite. Plagioclase is generally idiomorphic and shows tabular morphologies with aspect ratios of 1:2 to 1:6 (Fig. 4a). Most hornblende has polygonal morphologies and is often interstitial to plagioclase. In some cases, hornblende includes plagioclase as inclusions indicative of its later crystallization (Fig. 4a). Gabbro is mainly composed of plagioclase cumulates (> 60 vol%) and clinopyroxene with a closely-packed cumulate texture (Fig. 4b). Both clinopyroxene and plagioclase are medium in size and show xenomorphic to hypidiomorphic morphologies (Fig. 4b).

Phase II: The lower harzburgite in C–D cross-section (Fig. 3) displays a poikilitic texture with olivine cumulates (50–70 vol%) and interstitial plagioclase or orthopyroxene. Spinel, phlogopite and hornblende are accessory phases in the rock. Olivine is the only cumulus mineral and can be subdivided into two types according to the occurrences and morphologies: type I olivine is defined as inclusions in other silicates, e.g., pyroxene or plagioclase, showing polygonal or irregular morphologies (Fig. 4c); type II olivine has a discrete occurrence with embayed grain boundaries, without being included in any other

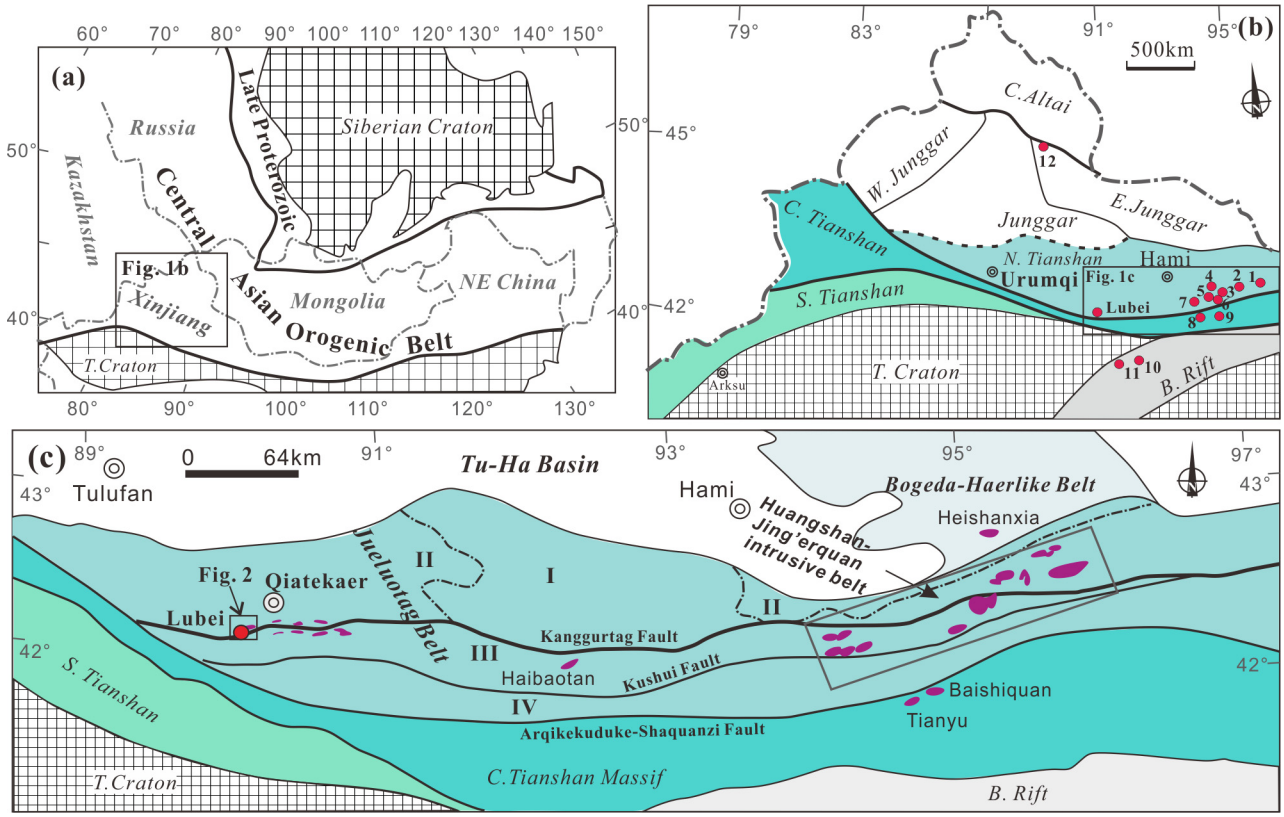

Fig. 1. (a) Simplified map of the CAOB (modified after Jahn, 2000); (b) tectonic framework and representative Ni–Cu sulfide ore deposits in North Xinjiang (modified after Song et al., 2011); (c) simplified geological map of the East Tianshan showing the distribution of Early Permian mafic–ultramafic intrusions (modified after Su et al., 2011). I – Dananhu–Tousuquan island arc terrane; II – Wutongwozi–Xiaorequanzi intra-arc basin; III – Kanggurtag intra-arc basin; IV – Aqishan–Yamansu arc terrane. C. Altai – Chinese Altai, N. Tianshan – Northern Tianshn, S. Tianshan – Southern Tianshan, C. Tianshan – Central Tianshan, W. Jungar – West Jungar, E. Jungar – East Jungar, T. Craton – Tarim Craton, B. Rift – Baishan Rift. **1** to **12** refer to magmatic Ni–Cu deposits in North Xinjiang: **1** – Tulargen, **2** – Hulu, **3** – Huangshandong, **4** – Xiangshan, **5** – Huangshanxi, **6** – Huangshannan, **7** – Tudun, **8** – Tianyu, **9** – Baishiquan, **10** – Poyi, **11** – Poshi and **12** – Kalatongke. Note that several non-involved mafic–ultramafic intrusions are not illustrated here.

silicates (Fig. 4d). Type I olivine may have crystallized *in situ* and was enclosed by subsequently crystallized pyroxene or plagioclase, while the type II may have crystallized during magma ascent, as indicated by their subrounded morphologies. The middle lherzolite also displays a poikilitic texture with olivine cumulates (> 60 vol%) and interstitial pyroxene (Fig. 4e). Most olivine was altered to Iddingsites and shows hypidiomorphic to sub-rounded morphologies with medium to coarse grain size (Fig. 4e).

Phase III: The top hornblende peridotite is characterized by a poikilitic texture with olivine cumulates (60–80 vol%) and interstitial hornblende (Fig. 4f), and lack of pyroxene or plagioclase. Olivine shows embayed morphologies with medium to coarse grain size (0.4–2.0 mm) and are much similar to the type I olivine in the lower harzburgite in crystal morphology (Fig. 4f). Hornblende is always interstitial to olivine and shows an optical continuity indicative of a magmatic origin. Presence of voluminous hornblendes in the hornblende peridotite suggests a water-enriched parental magma (Chen et al., 2018).

3.3. Ni–Cu mineralization

Seven Ni–Cu (Co) orebodies have been identified at the surface in the Lubei ore district, termed the Ni-1 to Ni-7 orebodies (Fig. 2). The Ni-1 orebody is the largest orebody in the Lubei district and is hosted by the southern ultramafic sub-intrusion, primarily strata-bound within harzburgite. It is ~800 m long and up to 164 m wide at the surface, striking NEE at ~80°, roughly consistent with the striking of the harzburgite layer at the surface (Fig. 2). Boreholes revealed that the thickness of the Ni-1 orebody was more than 80 m, dipping to the south at 30–50°. The supergene portion (~20 m undersurface) of the orebody was totally oxidized to limonite or malachite (Fig. 5a). The mineralized portion of the Ni-1 orebody, delineated by a cut-off grade of 0.2 wt% Cu and 0.2 wt% Ni, occupies ~30–40 vol% of the southern ultramafic sub-intrusion (Fig. 3b). The highest and average grades for Ni and Cu are 7.76 wt% and 0.72 wt%, 2.30 wt% and 0.48 wt%, respectively, with Co grades in the range of 0.01–0.034 wt%. The Ni-1 orebody contains > 80,000 t Ni, 30,000 t Cu and 1000 t Co resources (Xinjiang Geological Survey, 2014). The Ni-2 to Ni-5 orebodies are hosted by the central gabbro, showing subparallel strikings to each other (NEE, Fig. 2). The highest and average grades for Cu and Ni are 0.8 wt% and 0.3 wt%, 0.96 wt% and 0.26 wt%, respectively. Boreholes in the central gabbro failed to reveal the vertical extension of the four orebodies, and they were therefore viewed as uneconomic due to present exploration work. The Ni-6 orebody is the second largest orebody and is hosted by the fault along the southern contact between Carboniferous pyroclastic rocks and the northern hornblende gabbro (Fig. 2). It is ~1.2 km long and up to 50 m wide at the surface, striking SEE at 100°. It contains 0.2–1.4 wt% Cu and 0.2–0.9 wt% Ni. The Ni-7 orebody is hosted by a fault within the hornblende gabbro and shows a perpendicular striking to the Ni-6 orebody (N20°E, Fig. 2). It is ~600 m long with a maximum width of 70 m, containing 0.2–1.2 wt% Cu and 0.2–0.85 wt% Ni. The supergene portion of the Ni-6 and Ni-7 orebodies is mostly oxidized, and the vertical extensions of the two orebodies were unclear due to a lack of boreholes. Orebodies hosted by faults exclude a primary origin for the Ni-6 and Ni-7 orebodies but suggest injections of sulfide liquids fractionated from the parental magmas into the faults within hornblende gabbro. They are therefore viewed as vein sulfide ores in this

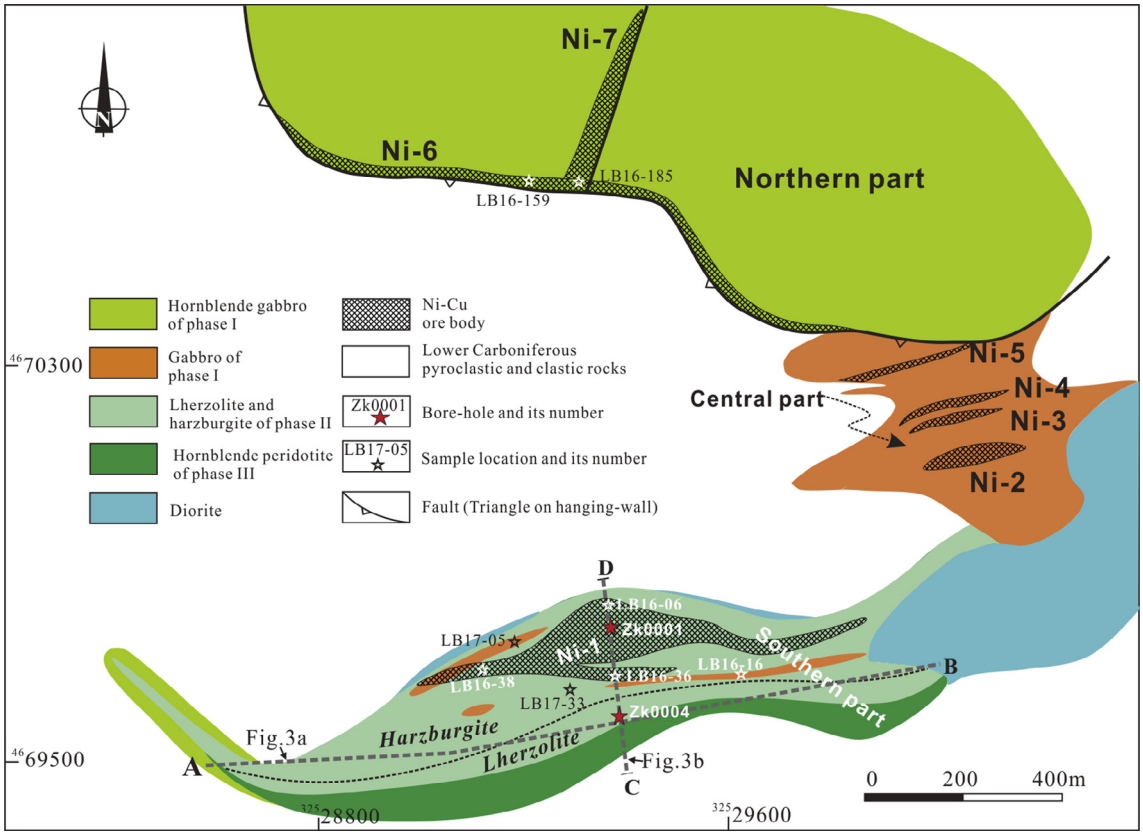

Fig. 2. Geological map showing the sample locations and the distributions of lithologic units and orebodies in the Lubei ore district (Modified from Xinjiang Geological Survey, 2014).

paper.

The oxidized ores of the Ni-6 and Ni-7 orebodies at the surface are mainly composed of nickeliferous magnetite (Fig. 5b) whilst a few primary ores contain tenorite, chalcopyrite, pyrite and minor pyrrhotite. The oxidized ores of the Ni-1 orebody at the surface are also composed of nickeliferous magnetite but still keep interstitial textures (Fig. 5c) as with the primary ones. Primary disseminated Ni–Cu sulfide ores (Fig. 5d) of the Ni-1 orebody, including sparsely (Fig. 5e) and densely disseminated sulfide ores (Fig. 5f), occur in the upper part of the harzburgite, grading downward into net-textured sulfide ores (Fig. 5g). Sulfides in the sparsely disseminated ores occur as blebs in the voids between olivine (Fig. 5e), and in the densely disseminated ores they connect together to form an interstitial texture (Fig. 5f). The net-textured ores contain more sulfides than the densely disseminated ores but sulfides in both of the two can have an interstitial texture. In some cases, silicates are immersed in sulfides in the net-textured ores (Fig. 5g). Primary sulfides include pyrrhotite, chalcopyrite, pentlandite, and pyrite. Nickeliferous pyrrhotite is the principal sulfide species that contain nickel, and chalcopyrite is the main sulfide species that contain copper.

In summary, primary sulfide ores only occur in the Lubei ultramafic rocks, including disseminated and net-textured sulfide ores. The oxidized ores of the Ni-6 and Ni-7 orebodies were likely resulted from an injection of a pulse of sulfide liquids fractionated from the Lubei

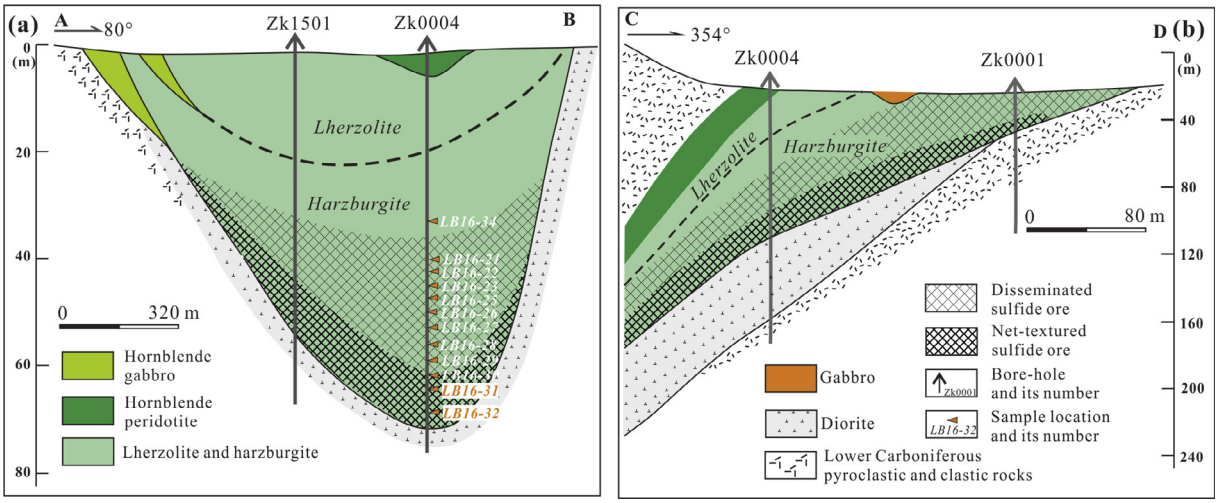

Fig. 3. A–B and C–D cross sections of the Lubei ultramafic sub-intrusion.

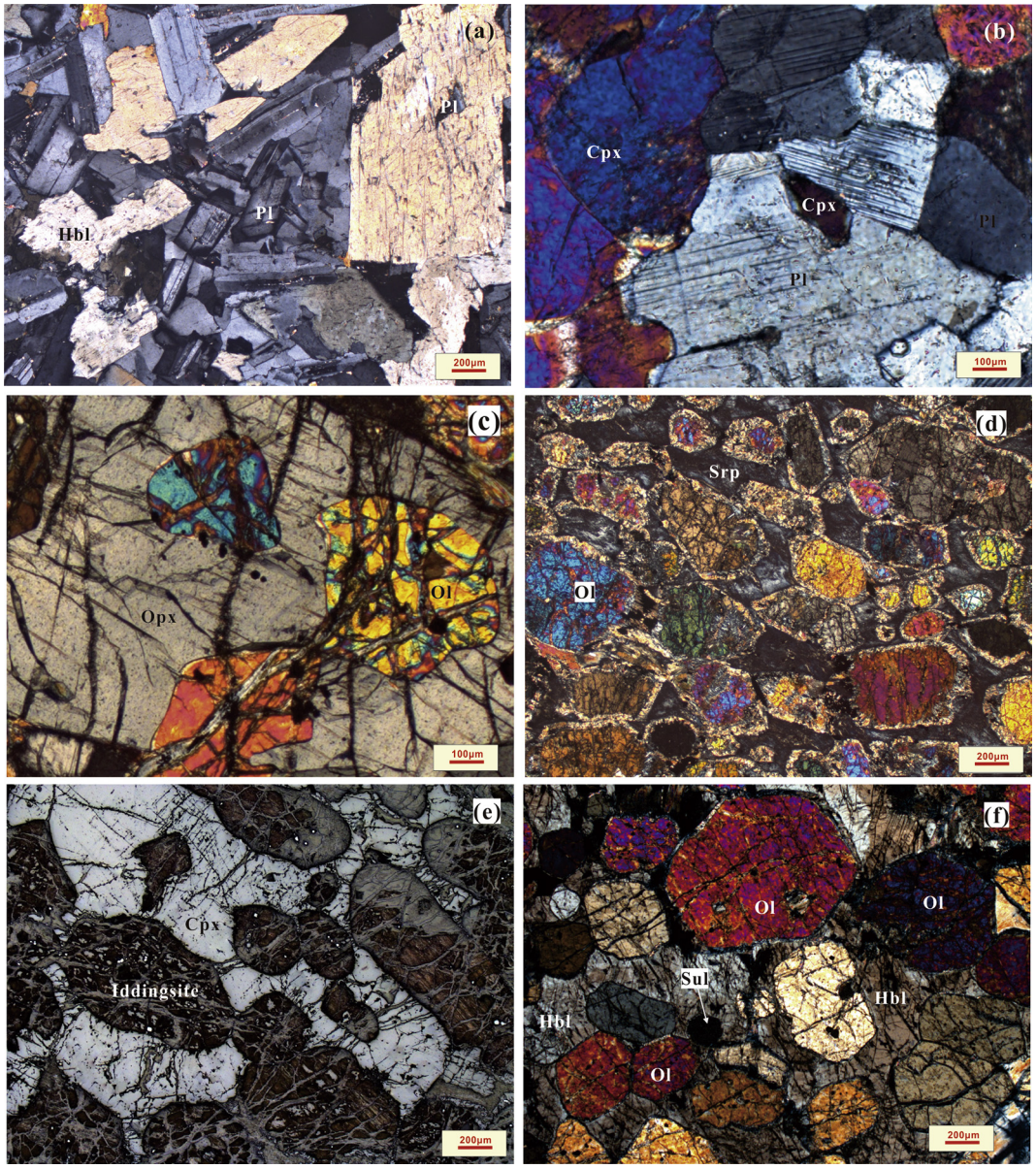

Fig. 4. Photomicrographs showing (a) cumulate texture of hornblende gabbro (cross-polarized light); (b) closely-packed cumulate texture of gabbro (cross-polarized light); (c) type-I olivine included in orthopyroxene in the harzburgite; (d) type-II olivine in the serpentinized harzburgite (cross-polarized light); (e) cumulus olivine and interstitial pyroxene in the lherzolite (reflected light); (f) cumulus olivine and interstitial hornblende in the hornblende peridotite. Abbreviations: Ol – olivine, Opx – orthopyroxene, Cpx – clinopyroxene, Pl – plagioclase, Srp – serpentine, Hbl – hornblende, Sul – sulfide.

parental magmas, namely vein sulfides.

4. Methods

4.1. Samples and analytical methods

The type-I olivine in three harzburgite samples, and sulfide and magnetite in four ore samples were selected for electron microprobe analysis (EMPA). Sample locations and numbers are shown in Figs. 2 and 3. The chemical compositions of minerals were determined by EMPA using a Jeol JXA-8230 microprobe at the Institute of Mineral Resources, Chinese Academy of Geological Sciences, Beijing, China. The operating conditions were accelerating voltage of 15 kV for silicate and oxide, and 20 kV for sulfide, beam current of 20 nA and beam size of 5 μm. Natural minerals and synthetic materials were used as standards, and all of the standards were tested for homogeneity before their utilization for quantitative analysis. Matrix corrections were carried out using the ZAF correction program supplied by the manufacturer.

Ten chalcopyrite, pyrite and pentlandite separates from seven disseminated and net-textured sulfide ores of the Ni-1 orebody in borehole Zk0004 were analyzed for sulfur isotopes. Sample locations and numbers are shown in Fig. 3a. Sulfur isotopic compositions were determined at the Analytical Laboratory, Beijing Research Institute of Uranium Geology, China National Nuclear Corporation, Beijing, China. Sulfide grains were mixed with cuprous oxide and crushed to 200 mesh. SO_2 was produced through the reaction of sulfide and cuprous oxide at 980 °C under vacuum (0.02 Pa) (Robinson and Kusakabe, 1975) and analyzed by mass spectrometry (MAT-251) for sulfur isotopes. Analytical uncertainties were better than ± 0.2‰.

Six disseminated and one net-textured sulfide ore samples were collected from the mineralized harzburgite in borehole Zk0004 (Fig. 3a), and they are the main primary ore species in the Lubei Ni-Cu sulfide ore deposit. Only one fresh mineralized sample from the Ni-6 orebody was collected because most sulfide ores in the Ni-6 and Ni-7

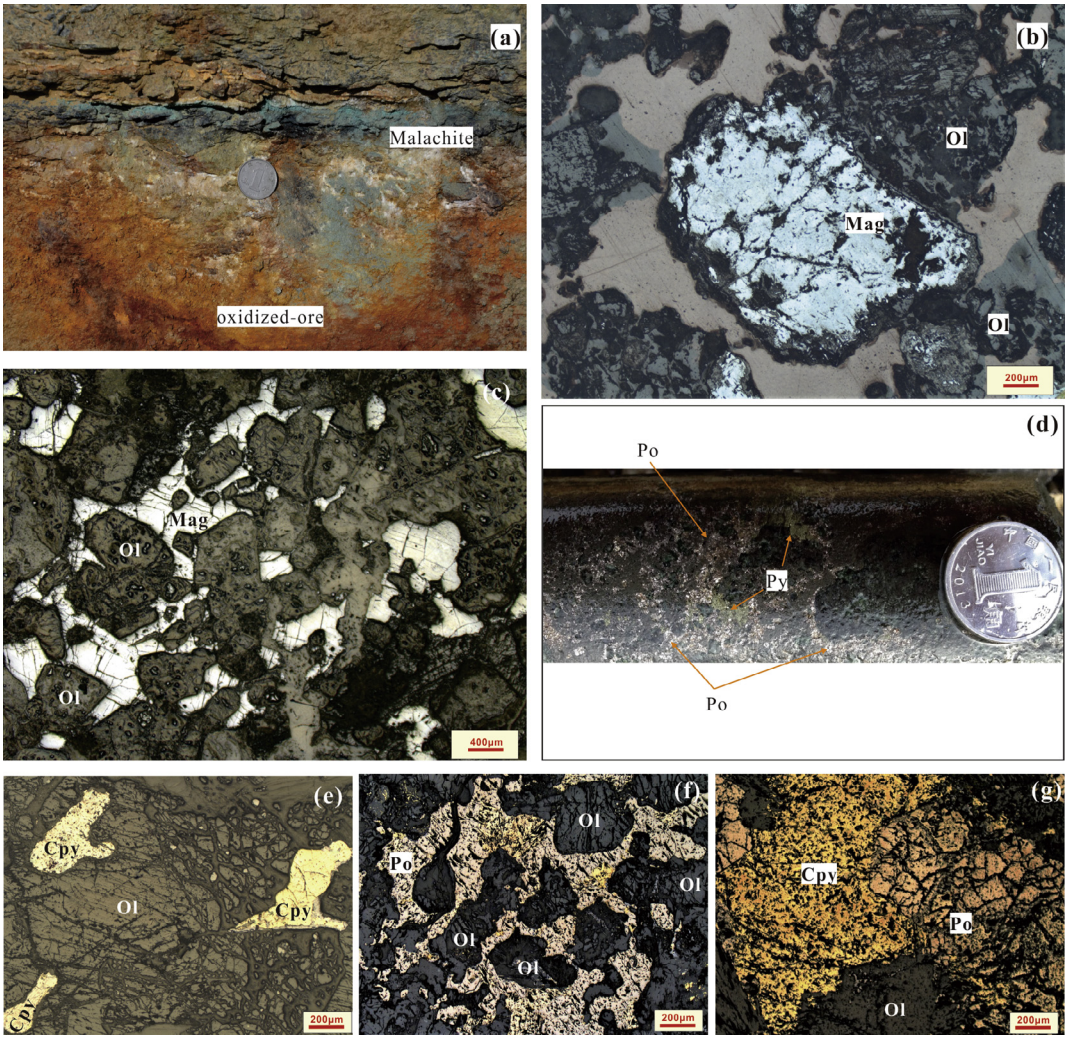

Fig. 5. (a) Field observation of oxidized ore at the surface. Photomicrographs showing (b) nickeliferous magnetite in the Ni-6 orebody (reflected light), (c) interstitial nickeliferous magnetite (oxidized portion of the Ni-1 orebody) (reflected light). (d) Drillcore showing disseminated sulfide ore. Photomicrographs showing (e) sulfide blebs in sparsely disseminated sulfide ore (reflected light), (f) densely disseminated sulfide ore (reflected light), (g) net-textured sulfide ore. Abbreviations: Po – pyrrhotite, Py – pyrite, Mag – Magnetite, others are shown in Fig. 4.

orebodies were oxidized at the surface. It therefore represents the vein sulfide ores in the Lubei Ni-Cu sulfide ore deposit. These mineralized samples together with two sulfide-poor gabbro samples were selected for whole-rock S, Cu, Ni, Co, and PGE analyses. Sample locations and numbers are shown in Figs. 2 and 3a. Whole-rock sulfur content in ores was analyzed at the National Research Center of Geoanalysis, Chinese Academy of Geological Sciences, Beijing, China, using the gravimetric method and IR-absorption spectrometry. Whole-rock PGE analyses were performed by nickel sulfide fire assay and Te coprecipitation at the National Research Center of Geoanalysis, Chinese Academy of Geological Sciences, Beijing, China, using the methods described by Asif and Parry (1991). Precision and accuracy indicated by reference material analysis (UMT-1 and WPR-1) were better than 10%. Blanks generally yielded PGE < 1 ppb, Ir < 0.15 ppb, Ru < 0.15 ppb, Rh < 0.05 ppb, Pt < 0.5 ppb, and Pd < 0.5 ppb. Cr, Ni, Cu, and Co abundances were determined by inductively coupled plasma–mass spectrometry (ICP–MS) following the method of Dulski (1994). Uncertainties were generally 3–5%, and precisions are based on averages of repeated analyses of standard BHVO-1. We also compiled Cu, Ni, Co, Pt, Pd, Au, Ag, Se, and Te data from Tian et al. (2017). These data are listed in Supplementary Table 1 (Table S1).

4.2. Method for the pMELTS modeling of partial mantle melting

Partial mantle melting is a significant factor that controls the Cu, Ni and PGE contents in magmatic sulfides and is discussed below. For simulation of partial melting of a hydrous mantle during post-collisional extension, the silicate-liquid model pMELTS is a suitable tool because it considers water content and pressure (1–3 GPa) (Naldrett, 2011; Ghiorso et al., 2013). The pMELTS modeling will yield a series of melts with different compositions depending on pressure, temperature, oxygen fugacity (fO_2) and H_2O content when the mantle composition is known. As to an adiabatic-decompression partial-melting regime, the pressure is the only variables and the temperature, fO_2 and H_2O content are given values. Changing the given temperature and H_2O content, respectively, the pMELTS modeling will correspondingly yield different melt compositions, and the degree of partial mantle melting will thus be determined by comparing the melt compositions with a well-determined primary magma composition.

It has been suggested that Early Permian mafic–ultramafic intrusions in the southern CAOB formed in a post-collision extensional tectonic setting, and the mantle source was hydrous due to previous metasomatism during Paleozoic subduction (Zhou et al., 2004; Song and Li, 2009; Song et al., 2011; Ren et al., 2014; Chen et al., 2018). It is thus reasonable to carry out the simulation of partial mantle melting based

Table 1
The compositions of olivine in Phase II harzburgite from the Lubei mafic–ultramafic intrusion.

Sample No.	Rock type	SiO_2	MgO	FeO	CaO	MnO	TiO_2	NiO	Cr_2O_3	Total	Ni	Ca	Fo
		wt%									ppm		%
LB16-25-1-3	Harzburgite	40.08	45.45	13.55	u.d	0.04	u.d	0.14	0.01	99.37	1084	u.d	85.67
LB16-25-1-4		40.59	44.68	14.17	0.03	0.09	0.10	0.13	0.01	99.83	990	186	84.90
LB16-25-3-4		40.85	44.40	15.03	u.d	0.04	0.00	0.14	0.05	100.58	1108	u.d	84.04
LB16-25-P3-1		38.72	45.63	14.04	0.08	0.07	0.10	0.18	0.01	99.08	1407	557	85.28
LB16-25-P3-2		39.74	45.10	14.41	0.07	0.08	0.00	0.16	0.01	99.61	1226	522	84.80
LB16-25-P3-4		40.00	45.33	13.98	0.05	0.04	0.01	0.20	0.03	99.65	1572	372	85.25
LB16-25-2-1		40.49	44.27	14.01	u.d	0.07	u.d	0.18	u.d	99.33	1375	u.d	84.93
LB16-25-2-2		39.88	44.59	14.95	0.01	0.08	u.d	0.14	0.04	99.76	1061	43	84.17
LB16-25-2-3		40.00	44.93	14.04	0.02	0.08	0.16	0.14	u.d	99.61	1061	107	85.08
LB16-23-1-3		39.89	44.93	13.09	0.03	0.10	0.00	0.12	u.d	98.24	943	179	85.95
LB16-23-1-4		40.25	45.65	14.31	0.02	0.08	0.03	0.11	0.01	100.55	888	150	85.04
LB16-23-2-3		40.17	43.70	15.07	0.02	0.10	0.05	0.15	0.01	99.34	1187	121	83.79
LB16-23-2-4		39.62	43.28	15.39	0.01	u.d	0.05	0.14	u.d	98.72	1092	57	83.37
LB16-23-3-2		39.12	44.52	13.87	0.03	0.06	0.00	0.12	0.08	97.86	935	236	85.12
LB17-33-2-2		40.11	44.59	14.42	0.02	0.06	0.00	0.12	0.01	99.41	912	157	84.65
LB17-33-1-5		40.40	43.50	13.22	0.07	0.02	0.03	0.14	0.03	97.61	1100	529	85.44
LB17-33-4-3		39.73	44.15	14.35	0.02	0.06	u.d	0.09	0.04	98.57	668	150	84.58
LB17-33-3-1		40.59	44.59	14.45	0.03	0.11	0.00	0.13	0.05	100.05	1029	222	84.61
LB17-33-3-2		39.84	43.27	14.17	0.02	0.02	0.05	0.12	0.05	97.58	943	121	84.48

Fo = 100 × Mg/(Mg + Fe^{2+}), atomic ratio. u.d = under detection limit.

on an adiabatic-decompression partial-melting regime with a hydrous mantle of variable H_2O content. The H_2O content of the mantle source was assumed to be similar to the arc mantle wedge which generally contains 0.01–0.5 wt% H_2O (Kelley et al., 2006; Kelley et al., 2010). The major element compositions of a generally-accepted depleted mantle source of Workman and Hart (2005) were selected as the starting compositions in the pMELTS modeling for the following reasons: (1) a depleted mantle source existed in the Early Permian in the southern CAOB due to previous extraction of arc or mid-ocean-ridge basaltic magmas during Paleo-Asian ocean evolution (Xiao et al., 2004; Ren et al., 2014; Kröner et al., 2017); (2) mantle spinel harzburgite has been identified in the western part of the East Tianshan (Li et al., 2008; Chen et al., in press), implying a depleted peridotite mantle source rather than pyroxenite beneath the East Tianshan region. However, these mantle rocks were severely serpentinized or impregnated by exotic melts (Li et al., 2008; Chen et al., in press) and were thus excluded as the starting compositions of the mantle source in this study; (3) a generally-accepted depleted mantle source of Hart and Zindler (1986) was also used in the pMELTS modeling by Naldrett (2011). As to ultramafic rocks with a poikilitic texture comprising olivine cumulates and other interstitial silicates such as plagioclase and pyroxene, the parental magma compositions can be calculated according to the mass balance method exploited by Li and Ripley (2011). The Lubei parental magma composition was thus calculated using this method and was reported by Chen et al. (2018). However, the Lubei parental magmas were fractionates of the primary magmas because the most primitive olivine in the Lubei ultramafic rocks had a lower Fo_{86} than 90 mol%. The primary magma composition was thus estimated by incrementally adding olivine with $Fo_{86–90}$ to the parental magmas until its composition was in equilibrium with olivine of Fo_{90} (Sun et al., 2013; Mao et al., 2015; Chen et al., 2018). The primary magma compositions used in this study are 50.0 wt% SiO_2, 11.6 wt% MgO, and 16.0 wt% Al_2O_3, and other major elements were reported by Chen et al. (2018). The calculated primary magma compositions are reliable in that they are consistent with the primary magma compositions of the Early Permian Huangshandong and Erhongwa mafic–ultramafic intrusions occurring along the Kanggurtag fault in the East Tianshan region (Sun et al., 2013; Mao et al., 2015). Oxygen fugacity was set at QFM-1 (one log unit below the fayalite–magnetite–quartz reference oxygen buffer) in this modeling. This value is generally stable for spinel peridotite at shallow depths of the upper mantle, generally less than 80 km (Woodland et al., 1990; Woodland and Koch, 2003) and was also employed by Naldrett (2011) in modeling partial mantle melting using pMELTS.

In this study, the modeling comprised two parts, i.e., Model A and Model B. Model A assumed an anhydrous mantle with temperature decreasing from 1450 to 1100 °C, which is within the temperature range of the upper mantle (1100–1500 °C, Thompson et al., 1992). At the beginning, pMELTS was run volatile-free at a set temperature of 1450 °C with a continuously decreasing pressure (0.1 kbar decrements) from 20 to 10 kbar (corresponding to mantle depths of ~66–33 km). Modeled melt compositions were then compared with those of the Lubei primary magmas (Chen et al., 2018). These procedures were repeated until the set temperature decreased to 1100 °C. Model B assumed a hydrous mantle with H_2O contents ranging from 0.1 to 0.5 wt%, similar to the H_2O contents in the arc mantle wedge (0.01–0.5 wt%; Kelley et al., 2006; Kelley et al., 2010). Other parameters were set similarly to those of Model A. Modeled melt compositions were compared with those of the Lubei primary magmas at a temperature range of 1450–1100 °C and at a H_2O content range of 0.1–0.5 wt%.

5. Analytical and modeling results

5.1. Mineral chemistry

Compositions of type-II olivine from phase III were reported by Chen et al. (2018). Type-I olivine from phase II harzburgite has forsterite contents [Fo = 100 × Mg/(Mg + Fe^{2+})$_{atomic}$] in the range of 83.4–86.0 mol. % and Ni contents of 668–1572 ppm with an average value of 1083 ppm (Table 1), lower than those from the hornblende peridotite of phase III (Fo = 84.6–86.1 mol. %, Ni = 1116–1658 ppm; Chen et al., 2018).

Representative compositions of sulfide in ores obtained by EMPA are listed in Table 2, and compositions of nickeliferous magnetite from the oxidized Ni-6 orebody are listed in Table 3. Chalcopyrite from the Ni-1 orebody is characterized by Cu content in a narrow range of 34.7–35.0 wt%. Cotectic pentlandite contains 39.4 wt% S, 21.8 wt% Fe and 36.3 wt% Ni. The oxidized ores of the Ni-6 orebody at the surface contain nickeliferous magnetite with 1.3–2.2 wt% CuO and 1.7–3.6 wt % NiO (Table 3).

5.2. Sulfur isotopes

The $\delta^{34}S$ values of the sulfides from the Lubei sulfide ore deposit vary within a narrow range of −0.3 to +1.8‰ (Table 4) and are in the

Table 2
The compositions of sulfides in ores from the Lubei mafic–ultramafic intrusion.

Sample	Sulfide	S	Zn	Co	Fe	Cu	Ni	Total	Cu/Fe	Fe/S	Cu/S
Sulfide ore (wt %)											
LB16-25-2-1	Chalcopyrite	35.00	0.02	0.03	30.03	34.49	0.00	99.60	1.1	0.9	1.0
LB16-25-2-2	Pyrite	38.83	0.02	0.08	60.05	0.06	0.00	99.08	0.0	1.5	0.0
LB16-32-5-1	Chalcopyrite	34.65	0.08	0.02	30.31	34.68	0.00	99.81	1.1	0.9	1.0
LB16-32-5-2	Pentlandite	39.43	0.00	0.72	21.77	0.72	36.32	98.98	0.0	0.6	0.0
LB16-06-1-1	Chalcopyrite	34.73	0.00	0.06	30.74	34.17	0.00	99.77	1.1	0.9	1.0
LB16-06-1-4	Chalcopyrite	34.40	0.12	0.06	30.41	34.29	0.00	99.32	1.1	0.9	1.0
LB16-06-2-3	Chalcopyrite	34.53	0.12	0.04	30.31	34.59	0.00	99.67	1.1	0.9	1.0
LB16-06-2-4	Chalcopyrite	34.30	0.04	0.04	30.26	34.44	0.00	99.08	1.1	0.9	1.0
LB16-06-3-3	Chalcopyrite	34.77	0.07	0.01	30.14	35.01	0.00	100.06	1.2	0.9	1.0
LB16-06-3-4	Chalcopyrite	34.51	0.26	0.05	30.34	34.65	0.00	99.83	1.1	0.9	1.0

range of mantle-derived magma (−3 to +3‰; Ohmoto, 1986), consistent with those of the sulfides from the Kalatongke deposit (−0.3 to 1.8‰; Wang and Zhao, 1991) in the Chinese Altai, the Huangshannan (−0.4‰ to 0.8‰; Mao et al., 2017), Huangshandong and Huangshanxi (−0.8‰ to 2.8‰; Wang et al., 1987) deposits in East Tianshan (Fig. 6).

5.3. Chalcophile elements

The Lubei mineralized harzburgite and vein sulfide ores are depleted in PGE (ΣPGE = 1.7–106 ppb, Table 5). The sulfide compositions of the disseminated, net-textured and vein sulfide ores were recalculated to 100% sulfide according to the equation of Barnes and Lightfoot (2005). Before the recalculation, the contributions of Ni from olivine were corrected using the average Ni content of olivine and the olivine modal content in the same sample. The mantle-normalized Ni, Cu and PGE patterns of disseminated, net-textured and vein sulfides are shown in Fig. 7. Disseminated sulfides have higher metal tenors than net-textured and vein sulfides except for the Cu tenors (Fig. 7). Net-textured and vein sulfides have steeper Cu, Ni and PGE patterns than those of the disseminated sulfides (Fig. 7), reflecting that Cu and PPGE (Pt, Pd) are more enriched relative to IPGE (Pt, Pd, Ru, Rh) in net-textured and vein sulfides, but less enriched in disseminated sulfides. All samples have Cu/Pd ratios one to two orders of magnitude higher than those of mantle rocks (10^3–10^4, Barnes and Picard, 1993) whilst the net-textured and vein sulfides have the highest Cu/Pd ratios (8–20 × 10^5, Table 5 and Table S1). The sulfide-poor gabbro samples also have high Cu/Pd ratios of 0.43–0.98 × 10^5 and low ΣPGE contents of 1.26–7.02 ppb (Table 5).

5.4. Results from the pMELTS modeling

The modeled results from the Model A are listed in Table S2. Melt compositions predicted by Model A failed to match those of the Lubei primary magmas at 1450–1300 °C. No results would be obtained from the pMELTS modeling below 1300 °C at 20–10 kbar when the mantle is anhydrous. The modeled results from the Model B are listed in Tables S3 and S4. After comparison, melt compositions obtained at ~0.29 wt% H_2O (temperature = 1298.5 °C, pressure = 10.5–12 kbar) are broadly comparable with those of the Lubei primary magmas. Representative modeled results of 1400, 1350, 1298.5, 1250, and 1200 °C at 0.29 wt% H_2O are given in Table S3 and in MgO and Al_2O_3 vs SiO_2 diagrams (Fig. 8a, b). Representative modeled results of 0.1, 0.2, 0.29, 0.4, and 0.5 wt% H_2O at 1298.5 °C are listed in Table S4 and in MgO and Al_2O_3 vs SiO_2 diagrams (Fig. 8c, d). The Lubei primary magma compositions were plotted in the MgO and Al_2O_3 vs SiO_2 diagrams (Fig. 8a–d), and the appropriate degree of partial mantle melting was 13–17% with 16% being the best outcome (Tables S3 and S4). This modeling also predicts a H_2O content of 1.4–1.8 wt% in the Lubei primary magmas with 1.6 wt % being the best outcome (Tables S3 and S4).

6. Discussions

6.1. Implications from Ni, Cu and PGE chemistry

The Lubei Ni–Cu sulfide ore deposit is depleted in PGE (Table 5). Available sulfides in the mantle will be completely exhausted at > 25% partial mantle melting assuming an initial sulfur content of 250 ppm in the mantle (Keays, 1995; Barnes and Lightfoot, 2005). Although 13–17% partial mantle melting is relatively low regarding the 25%, recent studies show that low degree of partial melting (even less than 10%) of a metasomatized/hydrous mantle may have consumed the available sulfides to generate primary magmas enriched in Cu, Ni and PGE compared with melting of an anhydrous mantle (Song and Li, 2009; Naldrett, 2011). It has been proved that a metasomatized/hydrous mantle existed beneath the southern CAOB in the Early Permian (Zhou et al., 2004; Song and Li, 2009; Song et al., 2011; Chen et al., 2018), and the low PGE contents are therefore not likely attributed to a low degree of partial mantle melting. It was supposed that early sulfide segregation would be an important factor that resulted in the low PGE contents of the sulfide ores in the southern CAOB (Song and Li, 2009; Mao et al., 2015; Tang et al., 2014; Zhao et al., 2015a,b). Early sulfide segregation processes for the Lubei Ni–Cu deposit will be discussed in later section.

When normalized to 100% sulfide, vein and net-textured sulfides in the Lubei sulfide ores have lower PGE tenors than associated disseminated sulfides, and vein sulfides have the lowest PGE tenors (Fig. 7). This chemical feature can be interpreted that disseminated sulfides represent sulfide droplets that have interacted with silicate liquids for a long time and collected more Ni, Cu and PGE than net-textured and vein sulfides which may have interacted with silicate liquids for a short time (Barnes and Lightfoot, 2005). The vein sulfides hosted in the Ni-6 and Ni-7 orebodies may be fractionated from the

Table 3
The compositions of nickeliferous magnetite in ores from the oxidized Ni-6 orebody in the Lubei Ni–Cu deposit.

Sample		MgO	Al_2O_3	SiO_2	FeO	MnO	Cr_2O_3	NiO	CoO	CuO	Total
Oxidized ore (wt %)											
LB16-185-1-1	magnetite	0.18	0.26	4.59	73.61	0.15	0.03	1.67	0.14	2.12	82.76
LB16-185-1-2		0.19	0.17	5.24	66.16	0.07	0.04	3.57	0.13	2.11	77.74
LB16-185-3-1		0.78	0.32	3.01	75.33	0.07	0.02	1.81	0.24	1.27	82.85
LB16-185-3-2		0.84	1.54	11.27	62.62	0.25	0.04	2.04	0.14	2.19	81.03

Table 4
The sulfur isotopic compositions of sulfides from the Lubei primary sulfide ores.

Sample No.	Mineral	$\delta^{34}S_{V\text{-}CDT}$ (‰)	Geological description
LB16-21	Pyrrhotite	1.4	Disseminated sulfide ore in harzburgite
LB16-22	Pyrrhotite	0.8	Disseminated sulfide ore in harzburgite
LB16-23	Pyrite	1.2	Disseminated sulfide ore in harzburgite
LB16-23	Chalcopyrite	1.8	Disseminated sulfide ore in harzburgite
LB16-23	Pyrrhotite	0.1	Disseminated sulfide ore in harzburgite
LB16-26	Pyrrhotite	1.2	Disseminated sulfide ore in harzburgite
LB16-28	Pyrrhotite	0.7	Disseminated sulfide ore hosted by harzburgite
LB16-28	Pentlandite	-0.3	Disseminated sulfide ore hosted by harzburgite
LB16-30	Pyrrhotite	1.3	Net-textured sulfide ore in harzburgite
LB16-31	Chalcopyrite	1.3	Net-textured sulfide ore in harzburgite

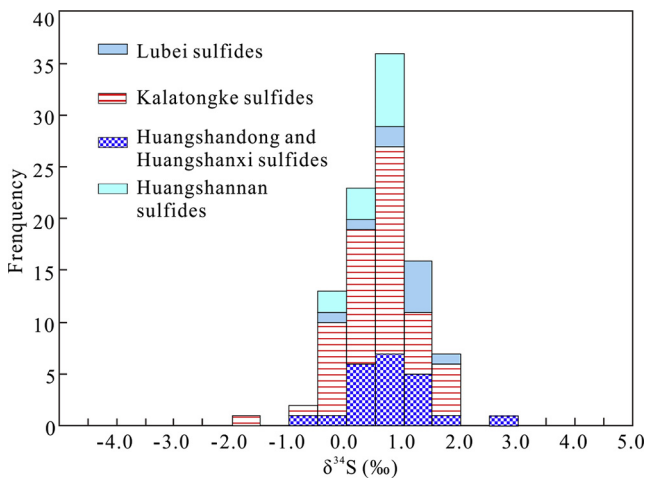

Fig. 6. Histograms of sulfur isotopic compositions for the Lubei, Huangshanxi, Huangshandong, Huangshannan and Kalatongke sulfide ores. Sulfur isotopes: Huangshanxi and Huangshandong (Wang et al., 1987), Huangshannan (Mao et al., 2017) and Kalatongke (Wang and Zhao, 1991).

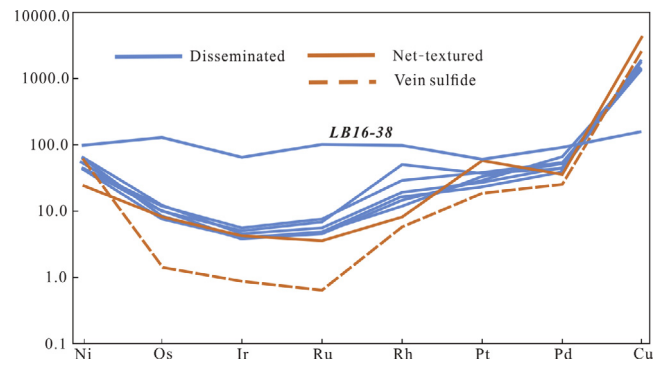

Fig. 7. Primitive mantle-normalized Cu, Ni and PGE patterns for 100% sulfide from the Lubei Ni–Cu sulfide ore deposit. The normalizing values are from McDonough and Sun (1995).

Lubei parental magmas and represent a pulse of sulfide liquids having the shortest interaction time with the silicate liquids. The Lubei sulfides have higher $(Pd/Ir)_N$ ratios (Primitive mantle normalized, McDonough and Sun, 1995) except for one sample (LB16-38) (Table 5). This high $(Pd/Ir)_N$ ratio reveals that the Lubei sulfide liquids possibly have undergone crystal fractionation of Fe-rich monosulfide solid solution (mss). Fe-rich mss was the first phase to crystalize from the sulfide liquids, and Cu and PPGE are strongly incompatible with it whilst IPGE are compatible (Barnes and Lightfoot, 2005). Crystal fractionation of Fe-rich mss from the Lubei sulfide liquids may have formed the observed metal compositions of the Lubei sulfides which are enriched in Cu and PPGE relative to IPGE. The sample LB16-38 shows a relatively flat pattern (Fig. 7) with lower $(Pd/Ir)_N$, and significantly, it may represent a kind of sulfide ores enriched in Fe-rich mss which were rarely identified in the Lubei district.

The Lubei sulfides have Cu/Pd ratios (10^4–10^5) one to two orders of magnitude higher than mantle values (10^3–10^4, Barnes and Picard, 1993). As Cu and PPGE are strongly incompatible with Fe-rich mss, crystal fractionation of Fe-rich mss from the sulfide liquids likely did not result in the high Cu/Pd ratios in the Lubei sulfides. Most Ni–Cu sulfide ore deposits in the southern CAOB, including those in North Xinjiang (Song and Li, 2009; Tang et al., 2011; Zhang et al., 2011; Mao et al., 2014, 2015, 2017; Wang et al., 2015; Zhao et al., 2015a,b) and the Hongqiling in Jilin province (Wei et al., 2013), are characterized by high Cu/Pd ratios (Fig. 9a–h, 10a–b and 11a; Table 6). Actually, many world-class Ni–Cu sulfide ore deposits which underwent early sulfide segregation would have obtained a high Cu/Pd ratio such as the Voisey's Bay in Canada, Jinchuan in China and Pechanga in Russia (Barnes and Lightfoot, 2005; Song and Li, 2009; Song et al., 2009; Lightfoot

Table 5
Sulfur and chalcophile element abundances of sulfide-poor gabbro and sulfide ores in the Lubei Ni–Cu sulfide ore deposit.

Sample No.	S	Os	Ir	Ru	Rh	Pt	Pd	Ni	Cu	Cr	Co	$(Pd/Ir)_N$	$(Pt/Pd)_N$	Cu/Pd	Geological description
	wt%	ppb						ppm							
LB16-16	0.01	0.11	0.06	0.06	0.08	0.37	0.58	276	57	784	49.9	8.22	0.36	98,276	Sulfide-poor gabbro
LB17-05	0.08	0.89	0.61	1.07	0.27	1.1	3.08	579	135	769	47.2	4.29	0.20	43,831	Sulfide-poor gabbro
LB16-38	0.42	4.79	2.42	5.52	1.02	4.75	4.03	2153	51.9	3022	114	1.42	0.67	128,783	Pentlandite-dominated disseminated ore in harzburgite
LB16-159	1.25	0.15	0.09	0.1	0.17	4.08	3.17	3704	2522	813	294	29.94	0.74	795,584	Vein sulfide ore in hornblende gabbro
LB16-27	0.20	0.19	0.09	0.18	0.13	1.26	1.02	1229	206	2031	102	9.63	0.71	201,961	Disseminated sulfide ore in harzburgite
LB16-34	0.24	0.27	0.1	0.18	0.12	1.24	1.17	1666	349	2169	108	9.95	0.61	298,291	Disseminated sulfide ore in harzburgite
LB16-36	0.11	0.1	0.05	0.1	0.14	0.77	0.52	1092	173	2311	118	8.84	0.85	332,692	Disseminated sulfide ore in harzburgite
LB16-25	0.77	0.59	0.27	0.48	0.29	4.25	5.61	3463	926	2330	175	17.66	0.43	165,062	Disseminated sulfide ore in harzburgite
LB16-29	0.50	0.32	0.17	0.3	0.14	2.93	2.59	1883	518	2112	117	12.95	0.65	200,000	Disseminated sulfide ore in harzburgite
LB16-32	6.32	4.82	2.45	3.09	1.36	69.6	24.6	8326	22,710	893	236	8.53	1.62	923,171	Net-textured sulfide ore in harzburgite

N: primitive mantle normalized (McDonough and Sun, 1995).

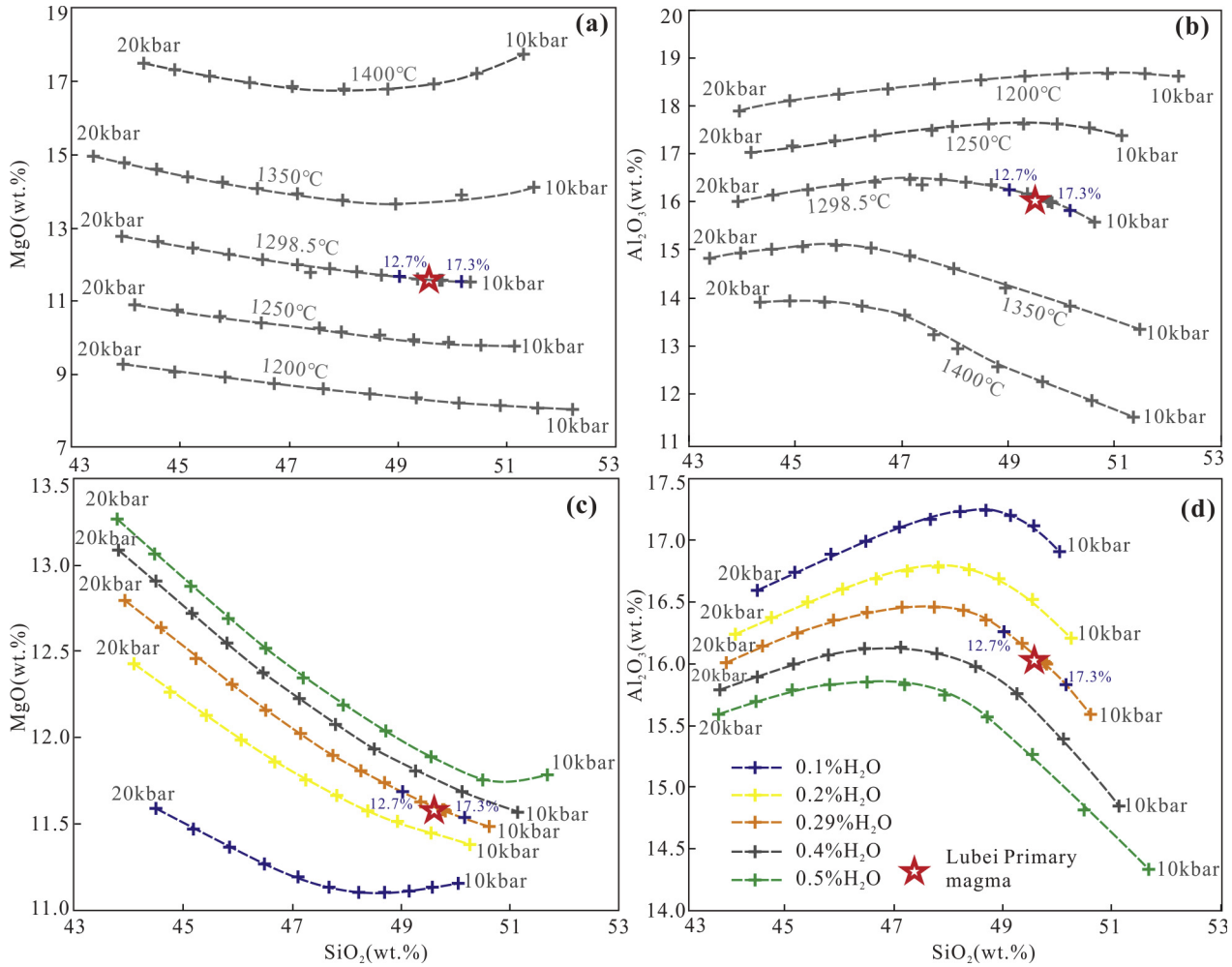

Fig. 8. Simulation of adiabatic-decompression partial melting of the hydrous mantle. (a) SiO_2 vs MgO, and (b) SiO_2 vs. Al_2O_3 showing modeling results from partial mantle melting with 0.29 wt% H_2O and continuously decreasing pressures from 20 to 10 kbar in 0.1 kbar decrements (changing the given temperature from 1450 °C to 1100 °C by 5 °C decrement). (c) SiO_2 vs MgO and (d) SiO_2 vs Al_2O_3 showing modeling results at 1298.5 °C with continuously decreasing pressures from 20 to 10 kbar in 0.1 kbar decrements, and with variable H_2O contents (0.1–0.5 wt%). The crosses represent primitive magma compositions obtained by the pMELTS modeling with variable degrees of partial mantle melting, as listed in Tables S3 and S4. The pentagram represents the compositions of the Lubei primary magmas. See text for further explanation.

et al., 2012), whereas those with no significant early sulfide segregation have lower Cu/Pd ratios such as the Noril'sk in Russia and Cape Smith in Canada (Barnes et al., 1997) (Fig. 10c, d; Table 6). Therefore, it appears that the low PGE contents of the Lubei sulfides as well as those in the southern CAOB were attributed to an early sulfide segregation process. This inference has been corroborated by the Kalatongke, Huangshandong, Huangshannan, Hulu, and Tianyu Ni–Cu sulfide ore deposits in North Xinjiang (Figs. 9a, b, e, h and 10a) and the Hongqiling Ni–Cu sulfide ore deposit in Jilin province (Fig. 10b; Song and Li, 2009; Wei et al., 2013; Deng et al., 2014; Zhao et al., 2015a,b). The southern CAOB, especially the North Xinjiang region, has a maximum crustal thickness of > 50 km in the Early Permian (Li et al., 2006) due to Paleozoic subduction and subsequent collision processes (Zhou et al., 2004). Such thickened crust could result in a unique magmatic system with long magma conduits, low magma velocity, and a significant temperature decrease, favoring early sulfide segregation. The observed widespread early sulfide segregation in Ni–Cu sulfide ore deposits in the southern CAOB is likely due to thickened crust and a distinct magmatic system.

6.2. Processes leading to ore formation

As stated above, early sulfide saturation and segregation had occurred in an earlier stage of the primary magma evolution. Following the early sulfide segregation, the parental magmas would have reached a second or *in situ* sulfide saturation, and the associated sulfide liquids would interact with silicate liquids (i.e., later sulfide–magma interaction). The second or *in situ* sulfide saturation was possibly related to magma crystallization, especially olivine fractionation.

6.2.1. Early sulfide segregation and later sulfide–magma interaction

The Lubei Ni–Cu sulfide ores contain sulfides, silicates, and minor oxides (Chen et al., 2018). Compared with sulfides, the silicates and oxides contain no significant Cu or Pd and do not significantly affect Cu/Pd ratios of the sulfide ores (Barnes and Picard, 1993; Barnes and Lightfoot, 2005). Hence, the Cu/Pd ratios of the Lubei sulfide ores can be employed to reveal the history of sulfide saturation and segregation. Early segregated sulfide liquids from the primary magmas have Cu/Pd ratios lower than that of the primary magmas whilst the residual magmas and later segregated sulfides will obtain a higher Cu/Pd ratio (Barnes and Picard, 1993). This is due to the fact that the partition coefficient of Pd between sulfide and silicate liquids (D_{Pd}) is much higher than that of Cu (D_{Cu}). D_{Pd} values are commonly in the range (2.0–8.8) × 10^4 and possibly > 10^7 (Fonseca et al., 2009), whereas D_{Cu} values are < 1.4 × 10^3 (Francis, 1990; Peach et al., 1990). Because the residual magmas are parental to the Lubei mafic–ultramafic rocks, they

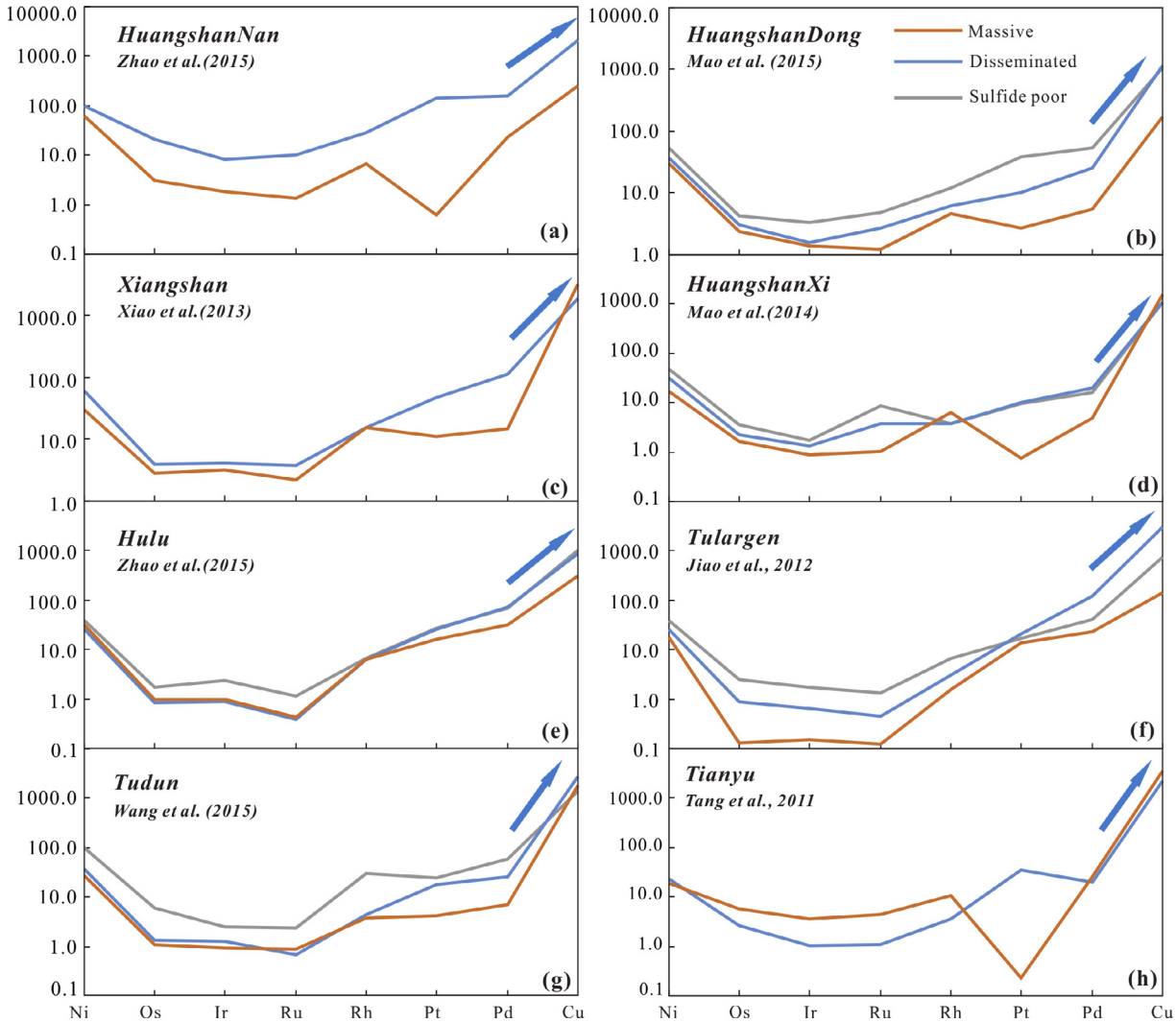

Fig. 9. Primitive mantle-normalized Cu, Ni and PGE patterns for 100% sulfide from deposits in East Tianshan.

are therefore referred to as parental magmas in this paper. Early sulfide segregation from the primary magmas would therefore cause a marked decrease in Pd content of the parental magmas, leaving Cu content relatively unchanged. Changes in metal contents of the parental magmas due to early sulfide segregation can be modeled using the equilibrium fractionation equation (Barnes and Picard, 1993):

$$C_i^{parental}/C_i^{primary} = 1/(1 + X(D_i - -1)/100), \quad (1)$$

where $C_i^{primary}$ is the initial concentration of element i in the primary magma; $C_i^{parental}$ is the final concentration of element i in the parental magma; D_i is the partition coefficient of element i between sulfide and silicate liquids; and X is the weight percent of segregated sulfide.

A batch partial melting model (Barnes and Lightfoot, 2005), applied with PGE contents of the upper mantle (McDonough and Sun, 1995), indicates that the Lubei primary magmas contained 95–116 ppm Cu, 276–380 ppm Ni and 4–10 ppb Pd at 13–17% partial mantle melting. Because the melt compositions obtained at 16% partial mantle melting highly approximate the Lubei primary magma compositions, the corresponding Cu (110 ppm) and Pd (6 ppb) contents were thus selected as the initial magma compositions for determining early sulfide losses. This composition is indicated as a grey star in the Cu/Pd vs Pd diagram (Fig. 11b). Changes in Cu/Pd ratios and Pd contents of the parental magmas, induced by increasing sulfide losses, were estimated using Eq. (1), and these changes are shown in Fig. 11b as a dashed line. The Lubei disseminated sulfide ores have higher Cu/Pd ratios than those of the primary magmas (Fig. 11b). This depletion in Pd relative to Cu is attributed to early sulfide losses from the primary magmas during ascent, and the proportion of early segregated sulfides was estimated to be at least 0.02 wt% (Fig. 11b). This proportion of segregated sulfides has largely depleted PGE and mediumly depleted Cu and Ni, leaving the parental magmas with 89.25 ppm Cu, 330 ppm Ni and 0.19 ppb Pd. Most Ni–Cu sulfide ores in North Xinjiang and Jilin province on the southern margin of the CAOB have high Cu/Pd ratios (Fig. 11a) and underwent early sulfide segregation processes such as the Huangshandong (extraction of > 0.012 wt% sulfides; Deng et al., 2014), Huangshannan (0.016 wt%; Zhao et al., 2015a), Hulu (0.0135 wt%; Zhao et al., 2015b), Tianyu (0.05 wt%; Tang et al., 2011), Kalatongke (0.018 wt%; Song and Li, 2009), and Hongqiling (0.2 wt%; Wei et al., 2013) Ni–Cu sulfide ore deposits (Table 6).

The parental magmas would reach second sulfide saturation progressively after early sulfide segregation, and sulfide liquids would inevitably interact with silicate liquids. This interaction would collect Cu, Ni and PGE from silicate liquids at different levels due to the high partition coefficients of these metals between sulfide and silicate liquids (Barnes and Picard, 1993; Barnes and Lightfoot, 2005). The enrichment of these metals during sulfide–magma interaction largely depends on the mass ratio of silicate to sulfide liquids, expressed as a R factor (Barnes and Picard, 1993). When the composition of the parental magmas is known, the R factor can thus be estimated, and the composition of sulfide ores can be modeled using the equilibrium

Table 6
Compiled Ni, Cu, S and PGE data of Ni-Cu sulfide ores from the deposits in the southern CAOB and several important deposits in the world.

Locations	Sample numbers	Sulfide types	S	Ni	Cu	Os	Ir	Ru	Rh	Pt	Pd	$(Pd/Pt)_N$	$(Pd/Ir)_N$	Cu/Pd	Early Sulfide segregation	Date sources
			wt%	ppb												
*Huangshannan	17	Diss.	2	18.7	6.1	72.3	28.5	49.1	27.1	990.8	636.2	18	304	96,169	0.016 wt%	Zhao et al. (2015a)
		Mass.	12	12.1	0.8	10.2	6.3	6.6	6.4	4.2	92.1	612	198	82,959		
*Huangshanxi	16	Sul.poor	0.5	9.4	3.2	12.3	5.9	42.7	3.6	66.0	65.2	28	150	489,510		Mao et al. (2014)
		Diss.	2.1	6.2	3.2	7.8	4.5	18.4	3.6	69.1	78.6	32	236	411,848		
		Mass.	14.7	3.3	4.5	5.5	3.0	5.2	6.0	5.4	19.7	102	89	2,303,619		
*Huangshandong	22	Sul.poor	0.24	10.6	3.1	14.3	11.5	24.1	11.3	270.4	210.4	1	23	160,827	0.012 wt%	Deng et al. (2014) and Mao et al. (2015)
		Diss.	4.60	7.1	3.5	10.4	5.3	13.4	5.8	72.8	100.2	2	21	725,567		
		Mass.	23.22	5.9	0.5	8.0	4.8	6.2	4.4	18.9	21.6	9	11	235,634		
*Tudun	11	Sul.poor	0.2	19.5	4.1	20.0	8.3	11.7	27.9	167.7	233.5	39	381	177,005		Wang et al. (2015)
		Diss.	4.8	7.2	8.3	4.5	4.4	3.4	4.3	124.5	102.9	23	317	804,511		
		Mass.	29.2	5.2	5.3	3.7	3.1	4.3	3.6	29.7	28.0	26	123	1,880,882		
*Hulu	28	Sul.poor	0.4	7.5	3.0	5.8	8.2	5.8	6.3	186.4	270.6	41	450	112,419	0.0135 wt%	Zhao et al. (2015b)
		Diss.	5.3	5.1	2.6	2.9	3.0	1.9	5.9	175.9	280.2	45	1285	91,690		
		Mass.	31.5	6.2	0.9	3.3	3.4	2.2	5.9	112.7	126.5	31	509	73,623		
*Xiangshan	9	Sul.poor	0.2	11.9	5.7	13.5	14.1	18.9	14.9	329.9	448.9	38	434	149,857		Xiao et al. (2013)
		Mass.	23.5	5.8	9.7	9.8	10.8	11.1	14.5	78.1	58.3	21	73	1,175,500		
*Tulargen	10	Sul.poor	0.5	7.5	2.2	8.5	6.0	6.6	6.4	118.9	161.8	38	367	135,029		Jiao et al. (2012)
		Diss.	3.9	4.9	9.0	3.1	2.2	2.3	2.9	146.5	480.8	92	2933	186,997		
		Mass.	25.7	6.7	0.4	0.0	0.5	0.6	1.5	94.9	89.9	27	2347	48,005		
*Lubei	10	Diss.	0.34	28.3	9.9	85.2	42.4	89.8	32.5	320.0	273.7	2	15	286,638	> 0.02 wt%	This study
		Mass.	6.32	4.9	13.3	28.1	14.3	18.0	7.9	406.1	143.5	1	10	923,171		
Karatongke China	13	Diss.	3.86	4.1	5.7	14.6	10.6	15.9	10.8	348.3	497.0	3	43	292,886	0.018 wt%	Song and Li (2009)
		Mass.	24.46	2.5	11.1	3.9	3.5	9.9	4.2	338.6	354.3	2	246	722,013		
*Tianyu	12	Diss.	4.37	4.6	6.5	9.1	3.5	5.3	3.3	247.0	77.9	17	29	1,251,210	> 0.05 wt%	Tang et al. (2011)
		Mass.	21.01	3.6	10.4	19.7	12.2	21.4	10.1	1.6	104.6	131	32	1,681,861		
Hongqiling China	18	Sul.poor	0.39	13.3	2.9	14.3	9.4	14.3	5.8	140.9	93.1	1	9	301,285	0.2 wt%	Wei et al. (2013)
		Diss.	5.45	7.8	5.1	3.7	2.0	2.9	1.9	29.9	14.9	1	10	3,995,658		
		Mass.	25.56	10.2	2.8	5.2	2.9	4.6	2.1	26.8	8.2	1	5	4,966,918		
Jinchuan China	45	Diss.	5.6	9.3	5.3	n.a.	142.7	242.6	86.7	474.0	1218.7	7	17	93,684	0.008 wt%	Song et al. (2009)
		Mass.	21.5	8.9	1.9	n.a.	32.5	69.5	24.1	35.6	257.0	69	12	106,405		
Pechenga Russia	37	Diss.	37.08	8.2	3.6	26	26	57	36	917	998	2	38	35,772	0.01 wt%	Barnes et al. (2001)
		Massive	37.24	9.4	2.1	63	47	103	57	333	417	2	9	49,640		
Voisey's bay Canada	46	Diss.	2.1	0.4	0.2	n.a.	0.4	1.0	0.8	7.5	21.8	82	826	71,469		Lightfoot et al. (2012)
		Massive	14.6	1.1	0.6	n.a.	3.0	9.0	5.7	7.7	51.7	187	232	112,477		
PMD Canada	12	Diss.	4.27	0.2	0.2	6.65	8.71	10.91	2.15	151.01	232.84	3	27	100,000	0.1–0.008 wt %	Sappin et al. (2011)
Noril'Sk Russia	44	Diss.	37.14	3.4	13.4	57	46	136	321	6808	25,184	7	547	5309		Barnes et al. (1997)
		Mass.	37.24	3.6	12.3	30	24	63	259	9421	29,049	6	1210	4224		
Cape Smith Canada	146	Diss.	36.99	11.4	3.4	351	264	1553	625	3530	9581	5	36	3528		Barnes et al. (1997)
		Mass.	37.74	0.8	2.0	146	117	717	483	2052	3227	3	28	6043		

*Deposits in East Tianshan on the southern margin of the CAOB. Notes: the average metal values were reported recalculated to 100% sulfides, n.a. = no analyses; Sul.poor = sulfide poor; Diss. = Disseminated sulfide ores; Mass. = Massive sulfide ores. N: primitive mantle-normalized (McDonough and Sun, 1995).

fractionation equation (Campbell and Naldrett, 1979):

$$C_i^{sulfide}/C_i^{silicate} = D_i(R + 1)/(R + D_i) \quad (2)$$

where $C_i^{sulfide}$ is the concentration of element i in sulfide liquid, $C_i^{silicate}$ is the concentration of element i in silicate liquid, D_i is the partition coefficient of element i between sulfide and silicate liquids, and R is the mass ratio of silicate to sulfide liquids, which quantifies the relative amount of magma that reacts with sulfide liquid (Barnes and Picard, 1993).

Calculations using Eq. (1) indicate that 89.25 ppm Cu, 330 ppm Ni and 0.19 ppb Pd remained in the Lubei parental magmas after early sulfide losses of 0.02 wt% from the Lubei primary magmas. Based on Eq. (2) and the Cu and Pd contents of the parental magmas, the Cu/Pd ratio varies as a function of R factor and Pd content as shown in Fig. 11b. The composition of most disseminated sulfide ores in the Lubei Ni–Cu sulfide ore deposit was quite well modeled at various R factors of 100–1000 except for two samples having a R factor of 5000–10,000 (Fig. 11b). These values are similar to those of the

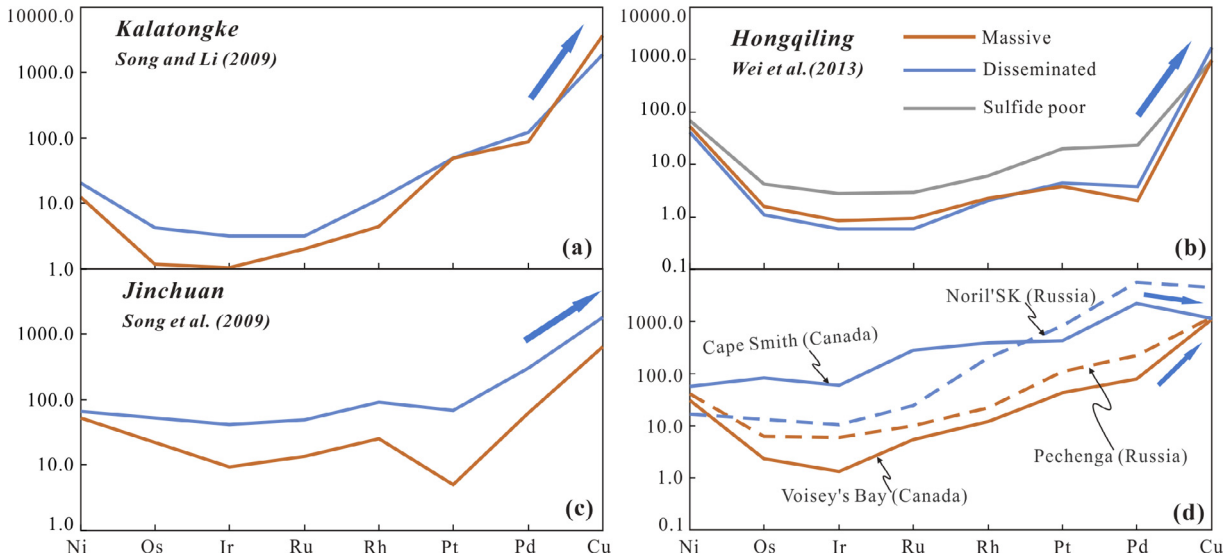

Fig. 10. Primitive mantle-normalized Cu, Ni and PGE patterns for 100% sulfide from the Kalatongke (Song and Li, 2009), Hongqiling (Wei et al., 2013), Jinchuan (Song et al., 2009), Noril'sk (Barnes et al., 1997), Pechenga (Barnes et al., 2001), Voisey's Bay (Naldrett et al., 2000), and Cape Smith Ni–Cu sulfide ore deposits (Barnes et al., 1997).

Huangshandong (100–1000, Mao et al., 2015), Huangshannan (200–3000, Mao et al., 2017), Tudun (168–1080, Wang et al., 2015), and Hulu (200–1600, Tang et al., 2014) Ni–Cu sulfide ore deposits in East Tianshan. One disseminated sample (sample LB16-38) was poorly modeled (Fig. 11b), plotting below the grey star of the Lubei primary magmas, possibly because the sulfides were dominated by Fe-rich mss with low Cu and PPGE relative to IPGE (Table 5), as evidenced by the flat Cu, Ni and PGE pattern (Fig. 7). The vein and net-textured sulfides plotted higher than the disseminated sulfide ores with high Cu/Pd ratios in Fig. 11b, indicating a very low R factor revealing weak interaction between the sulfide and silicate liquids. This inference was also evidenced by the lower metal tenors of vein and net-textured sulfides

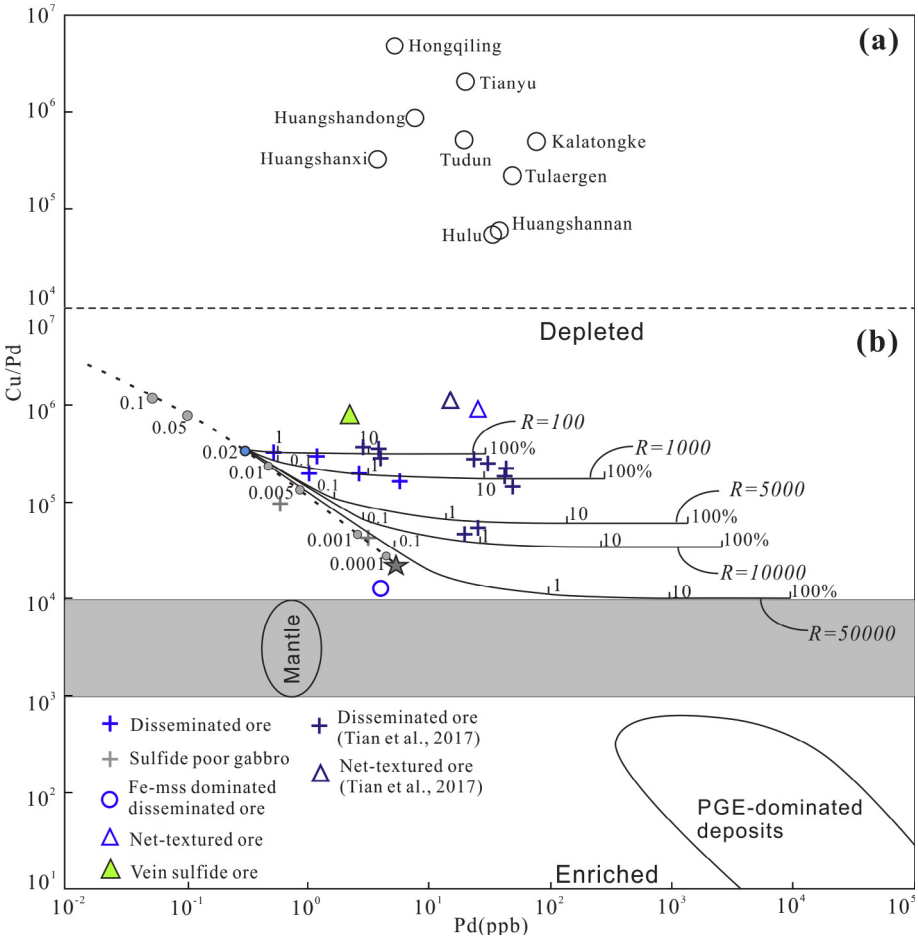

Fig. 11. (a) Plot of Cu/Pd vs Pd showing the distributions of Ni–Cu sulfide ore deposits in the southern CAOB. Date sources are the same as in Table 6; (b) plot of Cu/Pd ratio as a function of Pd showing the composition of the Lubei ultramafic rocks hosting disseminated to net-textured sulfide ores (based on Barnes and Picard, 1993). Values for the mantle and PGE-dominated deposits are from Barnes and Picard (1993). The gray star indicates the Lubei primary magma composition, derived from 13 to 17 % partial melting of a metasomatized mantle. The blue solid circle indicates the composition of the Lubei parental magmas after 0.02 wt% early sulfide losses from the Lubei primary magmas. The dashed line represents different proportions of sulfides segregated from the Lubei parental magmas. Solid lines link the silicate liquid and the sulfide in equilibrium with this silicate liquid for various R factors. Divisions on the solid lines indicate 0.1, 1, 10, and 100% sulfide in the rock. Data from Tian et al. (2017) are listed in Table S1. (For interpretation of the references to colour in this figure legend, the reader is referred to the web version of this article.)

than those of disseminated sulfides in the Lubei district (Fig. 7). The two sulfide-poor gabbro samples are plotted below the dashed line, suggesting phase-I gabbro rarely involved in the formation of the Lubei sulfide ores.

6.2.2. Relations of later sulfide saturation and olivine crystallization

Nickel is compatible with both olivine and sulfide (Keays, 1995; Li et al., 2003; Barnes and Lightfoot, 2005). Olivine would obtain a lower Ni content than expected when sulfides concurrently segregate from the parental magmas whilst the olivine Fo is left unchanged. The more sulfides saturated in the parental magmas, the lower Ni contents in olivine (Li et al., 2003, 2004, 2007). Therefore, the time and degree of sulfide saturation will be recorded at a Fo–Ni diagram revealing Fo–Ni variations of the associated olivine (Li et al., 2003, 2004, 2007). The detailed procedures to establish Fo–Ni variation can be found in Li et al. (2003, 2004, 2007).

The expected Fo variation of olivine against magma crystallization can be modeled using the silicate–liquid model MELTS (Ghiorso and Sack, 1995) (JAVA version 8 update 1.5.1) and the parental magma compositions. The estimated major elements of the Lubei parental magmas reported by Chen et al. (2018) were used as the initial magma compositions for the MELTS modeling. The initial H_2O content of the Lubei parental magmas was set at 1.6 wt%, assuming that the H_2O content was not significantly changed compared with the Lubei primary magmas. The oxygen fugacity (fO_2) in this modeling was calculated on the basis of hornblende compositions (Chen et al., 2018) according to the method of Ridolfi et al. (2010). The hornblende geothermometer (Ridolfi et al., 2010) yields a temperature range of 975–1019 °C for hornblendes in the Lubei ultramafic rocks indicative of a magmatic origin. The calculated fO_2 was in the range of 0.4–1.2 ΔNNO (0.4–1.2 log unit higher than the nickel–nickel oxide oxygen fugacity buffer) with an average value of 0.9, which was employed in this modeling. At the beginning, MELTS was applied at pressures of 1–9 kbar to obtain the most appropriate pressure at which this simulation would generate mineral assemblages petrographically matching the Lubei ultramafic rocks, with 2.4 kbar being the outcome (corresponding to a crustal depth of ~7 km). This simulation continued with a liquidus temperature range of 1310–1072 °C, decreasing in 0.5 °C decrements at 2.4 kbar. The degree of crystallization and the compositions of olivine and residual melts were observed at 2 °C temperature intervals, and are recorded at < 12 °C temperature intervals (Table S5). The modeled relationship between the olivine Fo content and the degree of crystallization at 2.4 kbar is given in Table S5. Nickel fractionation and its relationship with the degree of crystallization were modeled using the Rayleigh fractionation equation for trace elements (Barnes and Lightfoot, 2005; Li et al., 2007):

$$C_{Ni}^{residual} = C_{Ni}^{parental} * F^{(D--1)}, \quad (3)$$

where $C_{Ni}^{parental}$ is the concentration of Ni in the Lubei parental magma; $C_{Ni}^{residual}$ is the concentration of Ni in the residual liquid after fractionation of (1-F) vol. % spinel and olivine; F is the weight fraction liquid remaining; D is the bulk partition coefficient of Ni (D_{Ni}). D_{Ni} for spinel, olivine, orthopyroxene–clinopyroxene, and plagioclase in basaltic magmas were assumed to be 2, 7, 1, and 0, respectively (Li et al., 2003; https:// earthref.org), and D_{Ni} for immiscible sulfide liquid in basaltic magmas was assumed to be 500 (Naldrett, 2011; Mao et al., 2015). Modeled results are shown in Table S5.

Modeled Fo–Ni relations of olivine are shown in Fig. 12, where line *a* represents the expected spinel and olivine crystallization at various temperatures without sulfide saturation, based on the Lubei parental magma compositions (Chen et al., 2018) and an initial Ni content of 330 ppm calculated using Eq. (1). This is also an average Ni content of basaltic magmas (Li et al., 2004). This modeling thus predicts crystallization of spinel and $Fo_{86.9}$ olivine at a liquidus temperature of 1308 °C, followed by orthopyroxene at 1176 °C, plagioclase at 1114 °C, and clinopyroxene at 1084 °C (Fig. 12). The mineral assemblages and crystallization sequence are broadly comparable with the petrological observations of the Lubei ultramafic rocks (spinel → olivine → orthopyroxene → plagioclase/clinopyroxene → hornblende, Chen et al., 2018). The compositions of olivine from phases II and III of the Lubei ultramafic rocks plot below the model line a, indicating cotectic sulfide saturation with olivine and spinel crystallization. Model line *b* in Fig. 12 simulates olivine crystallization with cotectic sulfide saturation, with silicate to sulfide ratios in the range of 60–100 (Fig. 12). Voluminous *in situ* sulfide saturation occurs at 5–15 vol% magma crystallization, with the dominant silicates being olivine and spinel. Model dashed line *c* indicates olivine fractionation from the Ni-depleted magma (160 ppm Ni) after voluminous sulfide segregation (Fig. 12). Olivine from the phase II ultramafic rocks is more depleted in Ni than that from the phase III, with ratios of silicates to cotectic sulfides for the phase II being 60–80, and for the phase III 80–100 (Fig. 12). This indicates that the magmas of the phase II ultramafic rocks underwent more sulfide segregation than those of the phase III, with rocks of the two phases being formed from different magma pulses, as suggested by Chen et al. (2018).

6.2.3. The formation of the Lubei sulfide ores

The formation of the Lubei Ni–Cu sulfide ores is associated with the evolution of the Lubei primary magmas. The Lubei primary magmas were supposed to have evolved into two magma pluses in the deep magma chamber, one was more mafic (Mg# > 0.65) that formed the southern ultramafic sub-intrusion, and another was less mafic (Mg# < 0.6) that formed the central gabbro and northern hornblende gabbro (Chen et al., 2018). The ultramafic sub-intrusion hosts primary mineralization, and hence the formation of the Lubei sulfide ores is associated with the more mafic magma pulse.

The formation of the Lubei Ni–Cu sulfide ores includes two stages: (1) early sulfide segregation and (2) *later* sulfide saturation and separation, similar to the formation of the Huangshannan (Zhao et al., 2015a), Huangshandong (Mao et al., 2015), Hulu (Zhao et al., 2015b), Kalatongke (Song and Li, 2009) and Hongqiling (Wei et al., 2013) Ni–Cu sulfide ore deposits in the southern CAOB. In stage (1), the more mafic magma reached sulfide saturation at a lower level of the long magma conduit and lost at least 0.02 wt% sulfides from the Lubei primary magmas. These early formed sulfides either remained at depth or were injected into the lower crust (Fig. 13a), causing depletion of the parental magmas in metals, especially in PGE. In stage (2), the parental magmas reached second or *in situ* sulfide saturation during ascent, and metal depletion of these sulfides due to early sulfide losses was partially compensated by later sulfide–magma interaction with a R factor of 100–1000 (Fig. 13b). Most of the second sulfide liquids were settled downward when meeting a structural trap in the upper magma conduit with some sulfides escaping and inserting into the faults in hornblende gabbro to form the Ni-6 and Ni-7 orebodies (Fig. 13b). *In situ* fractionated sulfide liquids tend to descend and concentrate at a lower level of the structural trap due to their high gravity, consistent with the rising Ni (Cu) grades with depth in harzburgite in the Lubei Ni–Cu sulfide ore deposit (Fig. 3).

7. Implications for exploration

Most of the world's large magmatic sulfide deposits are interpreted to have formed in continental rift settings (Naldrett,1997; Naldrett, 1999; Maier et al., 2008), such as the Noril'SK in Russia (Lightfoot and Keays, 2005), Cape smith in Canada (Barnes et al., 1997), and Cu–Ni sulfide mineralization in the Duluth Complex (USA) (Ripley et al., 2007). An ideal site for the formation of these large ore deposits is where a mantle plume intersects a continental rift (Barnes and Lightfoot, 2005). The plume provides a large volume of magmas with high metal contents, produced by a high degree of partial melting. The normal faults of the rift provide easy access to the crust so that the

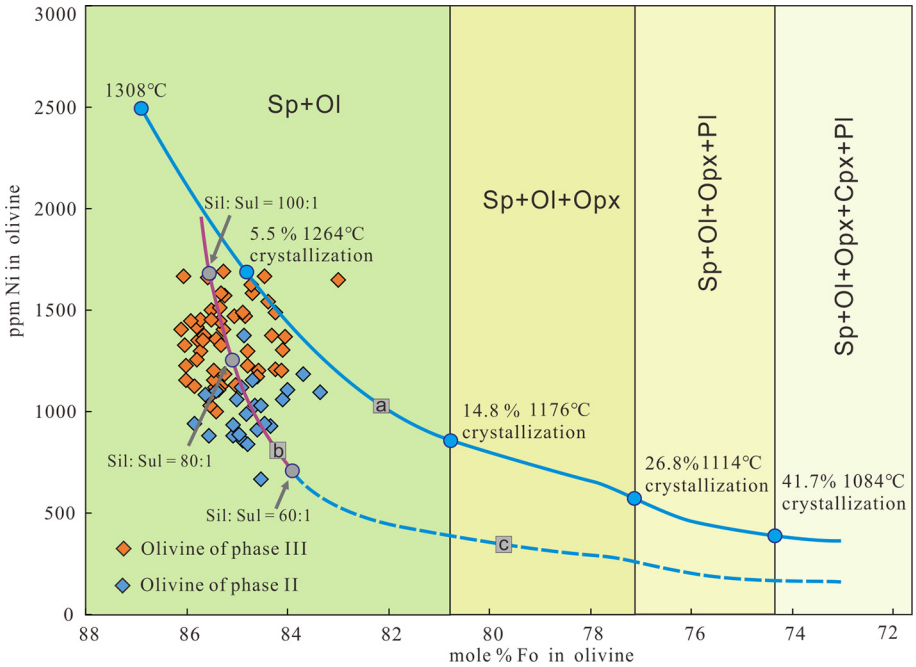

Fig. 12. Modeling of mineral fractionation of the Lubei ultramafic rocks from the Lubei parental magmas. The model line *a* represents expected olivine crystallization at various temperatures without sulfide saturation, using the compositions of the Lubei parental magmas (Chen et al., 2018) and an initial Ni content of 330 ppm calculated using Eq. (1). The model line *b* simulates olivine crystallization with cotectic sulfide saturation. The model dashed line *c* represents expected olivine fractionation from Ni-depleted magma (160 ppm Ni) after voluminous sulfide saturation and segregation. See text for explanations. Abbreviations: Sil – Silicates, Sul – Sulfide, Ol – olivine, Opx – orthopyroxene, Cpx – clinopyroxene, Sp – Spinel, Pl – plagioclase. The major element compositions of the Lubei parental magmas were given in Chen et al. (2018). The simulation of fractional crystallization was performed at 2.4 kbar and at 0.9 ΔNNO fO_2 using the silicate–liquid model MELTS of Ghiorso and Sack (1995) (JAVA version 8 update 1.5.1).

magma is transported efficiently (Barnes and Lightfoot, 2005), without significant early sulfide segregation.

Recently, many magmatic Ni–Cu sulfide ore deposits were discovered in orogenic settings or subduction-related magmatic arcs (Maier et al., 2008; Sappin et al., 2011), and they have significantly contributed to the Ni and Cu resources in China or the world, such as the Devonian Xiarihamu (157 Mt at 0.65 wt% Ni and 0.14 wt% Cu; Song et al., 2016) in Qinghai province (West China), the Early Permian Kalatongke (33 Mt at 0.8 wt% Ni and 1.3 wt% Cu; Song and Li, 2009) and Huangshan-Jing'erquan Ni–Cu belt (> 50 Mt at an average grade of 0.52 wt% Ni and 0.27 wt% Cu; Mao et al., 2015) in North Xinjiang (NW China), and the Early Carboniferous Ni–Cu ore deposits (16 Mt at 0.66 wt% Ni and 0.46% wt% Cu; Pina et al. 2006) hosted in the Aguablanca intrusion in Spain. The formation of these Ni–Cu deposits are distinct from that in rift settings in that (1) generation of mantle magmas is related to flux melting of mantle wedges overlying subduction zones (Maier et al., 2008) rather than mantle plumes, resulting in a low degree of partial mantle melting (Song and Li, 2009), (2) early sulfide segregation is more prevalent during magma ascent which would deplete the sulfide ores in chalcophile elements due to thickened crust (Barnes and Lightfoot, 2005), and (3) the predominantly compressive environments of orogenic belts may result in relatively few dilatant sites through which magmas can ascend, and orogenic belts tend to contain fewer S-bearing sedimentary strata than rifts (Maier et al., 2008).

The abovementioned factors appear unfavorable in making a giant magmatic Ni–Cu deposit. Nevertheless, the key factor that make an orogenic or post-subduction setting a good site for magmatic Ni–Cu sulfide ore deposits is a hydrous mantle accompanied by activation of translithospheric faults during post-collisional extension, because (1) water will lower the solidus temperature and arise the degree of partial mantle melting (Thompson, 1992), and (2) hydrous mantle magmas will dissolve much more sulfides from the source rocks than dry magmas even at a low degree of partial mantle melting (Song and Li, 2009). Post-collisional extension following subduction is also a requisite in the formation of magmatic Ni–Cu sulfide ore deposits because it would lead to activation of translithospheric faults and provide dilatant sites through which magmas can ascend. That is why most magmatic Ni–Cu deposits in the southern CAOB generally occur along translithospheric faults such as the Kalatongke along the Irtysh fault, the Tianyu and Baishiquan along the Arqikekuduke fault, and the Huangshan-Jing'erquan Ni–Cu ore belt along the Kanggurtag fault (Mao et al., 2008). Therefore, these translithospheric faults are still targets for Ni–Cu exploration in the southern CAOB. Base on the abovementioned analysis, except rift settings intersected by a mantle plume, another good site for the formation of magmatic Ni–Cu sulfide ore deposits is a post-subduction tectonic setting with a hydrous mantle accompanied by activation of translithospheric faults during post-collisional extension.

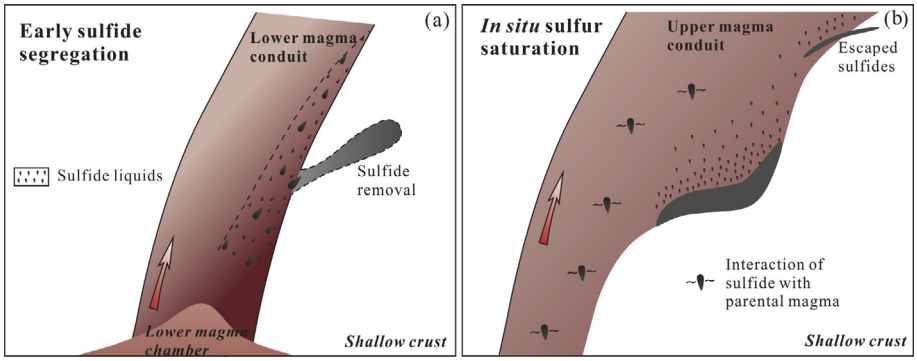

Fig. 13. Illustrations showing (a) early sulfide segregation from the Lubei primary magmas in the lower magma conduit; (b) second or *in situ* sulfide saturation in a structural trap in the upper magma conduit.

8. Conclusions

(1) The primary magmas responsible for the Lubei mafic–ultramafic intrusion were derived from 13 to 17 % partial mantle melting with a H_2O content of 0.29 wt% in the mantle. Early sulfide segregation played a significant role in depletion of the Lubei Ni–Cu sulfide ores in PGE.

(2) Two stages of sulfide segregation were involved in the formation of the Lubei sulfide ores during magma ascent. In stage (1), the primary magmas segregated at least 0.02 wt% sulfides in the lower magma conduit, leading to depletion of the parental magmas in chalcophile elements, especially in PGE. In stage (2), the parental magmas reached a second or *in situ* sulfide saturation, and the depletion of the second sulfides in chalcophile elements were then compensated by sulfide–magma interaction with an R factor of 100–1000. Orebodies hosted by the Lubei ultramafic rocks resulted from *in situ* sulfide saturation of the Lubei parental magmas, whereas a pulse of sulfide liquids, fractionated from the Lubei parental magmas in the upper magma conduit, was injected into faults in hornblende gabbro to form local orebodies.

(3) Another possible site for the formation of magmatic Ni–Cu deposits except rift settings is a post-subduction setting with a metasomatized/hydrous mantle accompanied by activation of translithospheric faults during post-collisional extension.

Acknowledgements

We thank Wang Junliang, Li Dahai, Zhang Xiaojun and Wang Cheng of Xinjiang Geological Survey for their support and assistance during fieldwork. We gratefully acknowledge constructive comments and helpful suggestions from Prof. Lightfoot P.C., Dr. David Holwell, Dr. Margaux Le Vaillant and one anonymous reviewer that improved earlier versions of the manuscript. This work was supported by the Geological Survey of China (DD20160007 and 12120115055601), the State Key Fundamental Program project (2012CB416803) and the National Natural Science Foundation of China (41372091).

Appendix A. Supplementary data

Supplementary data to this article can be found online at https://doi.org/10.1016/j.oregeorev.2018.11.017.

References

Asif, M., Parry, S.J., 1991. Study of the digestion of chromite during nickel sulfide fire assay for the platinum group elements and gold. Analyst 116, 1071–1073.
Barnes, S.J., Lightfoot, P.C., 2005. Formation of magmatic nickel-sulfide ore deposits and processes affecting their copper and platinum-group element contents. Econ. Geol. 100, 179–213.
Barnes, S.J., Melehik, V., Sokolov, S.V., 2001. The composition and mode of formation of the Pechenga nickel deposits, Kola Peninsular, northwestern Russia. Can. Mineral. 39, 447–472.
Barnes, S.J., Picard, C.P., 1993. The behaviour of platinum group elements during partial melting, crystal fractionation and sulfide segregation: an example from the Cape Smith fold belt, northern Quebec. Geochim. Cosmochim. Acta 57, 79–87.
Barnes, S.J., Zientek, M., Severson, M.J., 1997. Ni, Cu, Au and platinum group element contents of sulfides associated with intraplate magmatism: a synthesis. Can. J. Earth Sci. 34, 337–351.
Campbell, I.H., Naldrett, A.J., 1979. The influence of silicate:sulfide ratios on the geochemistry of magmatic sulfides. Econ. Geol. 74, 1503–1506.
Casquet, C., Galindo, C., Tornos, F., Velasco, F., Canales, A., 2001. The Aguablanca Cu–Ni ore deposit (Extremadura, Spain), a case of synorogenic orthomagmatic mineralization: age and isotope composition of magmas (Sr, Nd) and ore (S). Ore Geol. Rev. 18, 237–250.
Chen, B.Y., Yu, J.J., Liu, S.J., submitted for publication. Contributions of mantle basaltic magmatism to lower crustal growth in the Chinese Tianshan Orogenic Belt, North China. Gondwana Res.
Chen, B.Y., Yu, J.J., Liu, S.J., 2018. Source characteristics and tectonic setting of mafic–ultramafic intrusions in North Xinjiang, NW China: insights from the petrology and geochemistry of the Lubei mafic–ultramafic intrusion. Lithos 308–309, 329–345.
Deng, Y.F., Song, X.Y., Chen, L.M., Zhou, T., Pirajno, F., Yuan, F., Xie, W., Zhang, D., 2014. Geochemistry of the Huangshandong Ni–Cu deposit in northwestern China: implications for the formation of magmatic sulfide mineralization in orogenic belts. Ore Geol. Rev. 56, 181–198.
Dulski, P., 1994. Interferences of oxide, hydroxide and chloride species in the determination of rare earth elements in geological samples by inductively coupled plasma-mass spectrometry. Fresenius's J. Anal. Chem. 350, 194–203.
Fonseca, R.O.C., Campbell, I.H., O'Neill, H.S.T.C., Allen, C.M., 2009. Solubility of Pt in sulfide mattes: implications for the genesis of PGE-rich horizons in layered intrusions. Geoch. Cosmo Acta 73, 5764–5777.
Francis, R.D., 1990. Sulfide globules in mid-ocean ridge basalts (MORB), and the effect of oxygen abundance in Fe-S-O liquids on the ability of those liquids to partition metals from MORB and komatiite magmas. Chem. Geol. 85, 199–213.
Hart, S.R., Zindler, A., 1986. In search of a bulk-earth composition. Chem. Geol. 57 (3), 247–267.
Ghiorso, M.S., Hirschmann, M.M., Reiners, P.W., Kress, V.C., 2013. The pMELTS: a revision of MELTS for improved calculation of phase relations and major element partitioning related to partial melting of the mantle to 3 GPa. Geochem. Geophys. Geosyst. 3 (5), 1–35.
Ghiorso, M.S., Sack, R.O., 1995. Chemical mass transfer in magmatic processes IV. A revised and internally consistent thermodynamic model for the interpolation and extrapolation of liquid–solid equilibria in magmatic systems at elevated temperatures and pressures. Contrib. Miner. Petrol. 119, 197–212.
Jahn, B.M., 2000. Massive granitoid generation in Central Asia: Nd isotopic evidence and implication for continental growth in the Phanerozoic. Episodes 23 (2), 82–92.
Jiao, J.G., Tang, Z.L., Qian, Z.Z., Sun, T., Duan, J., Jiang, C.Y., 2012. Genesis and metallogenic process of Tulargen large scale Cu-Ni sulfide deposit in eastern Tianshan area, Xinjiang. , Acta Geologica Sina 28 (11), 3772–3786 (in Chinese with English abstract).
Keays, R.R., 1995. The role of komatiitic and picritic magmatism and S-saturation in the formation of ore deposits. Lithos 34 (1–3), 1–18.
Kelley, K.A., Plank, T., Newman, S., Stolper, E.M., Grove, T.L., Parman, S., Hauri, E.H., 2010. Mantle melting as a function of water content beneath the Mariana arc. J. Petrol. 51, 1711–1738.
Kelley, K.A., Terry, P., Grove, T.L., Stolper, E.M., Sally, N., Erik, H., 2006. Mantle melting as a function of water content beneath back–arc basins. J. Geophys. Res. Solid Earth 111 (B9), 1–27.
Kröner, A., Kovach, V., Alexeiev, D., Wang, K.L., Wong, J., Degtyarev, K., Kozakov, I., 2017. No excessive crustal growth in the Central Asian Orogenic Belt: further evidence from field relationships and isotopic data. Gondwana Res. 8 (3), 503–504.
Li, C.S., Naldrett, A.J., Ripley, E.M., 2007. Controls on the Fo and Ni contents of olivine in sulfide-bearing mafic/ultramafic intrusions: principles, modeling, and examples from Voisey's bay. Earth Sci. Front. 14 (5), 177–183.
Li, C.S., Ripley, E.M., 2011. The giant Jinchuan Ni–Cu-(PGE) deposit: tectonic setting, magma evolution, ore genesis and exploration implications. Rev. Econ. Geol. 17, 163–180.
Li, C.S., Ripley, E.M., Naldrett, A.J., 2003. Compositional variations of olivine and sulfur isotopes in the Noril'sk and Talnakh intrusions, Siberia: implications for ore-forming processes in dynamic magma conduits. Econ. Geol. 98, 69–86.
Li, C.S., Xu, Z., Waal, S.A.D., Ripley, E.M., Maier, W.D., 2004. Compositional variations of olivine from the Jinchuan Ni–Cu sulfide deposit, western China: implications for ore genesis. Miner. Deposita 39 (2), 159–172.
Li, C.S., Zhang, Z.W., Li, W.Y., Wang, Y.L., Sun, T., Ripley, E.M., 2015. Geochronology, petrology and Hf–S isotope geochemistry of the newly-discovered Xiarihamu magmatic Ni–Cu sulfide deposit in the Qinghai-Tibet plateau, western China. Lithos 216–217, 224–240.
Li, J.X., He, G., Xu, X., Li, H., Sun, G., Yang, T., 2006. Crustal tectonic framework of northern Xinjiang and adjacent regions and its formation. Acta Geol. Sin. 80 (1), 148–168.
Li, W.Q., Ma, H.D., Wang, R., Wang, H., Xia, B., 2008. SHRIMP dating and Nd–Sr isotopic tracing of Kanggurtag ophiolite in eastern Tianshan, Xinjiang. Acta Petrologica Sinica 24 (4), 773–780.
Lightfoot, P.C., Evans-Lamswood, D., 2015. Structural controls on the primary distribution of mafic–ultramafic intrusions containing Ni–Cu–Co–(PGE) sulfide mineralization in the roots of large igneous provinces. Ore Geol. Rev. 64, 354–386.
Lightfoot, P.C., Keays, R.R., 2005. Siderophile and chalcophile metal variations in flood basalts from the Siberian trap, Noril'sk region: Implications for the origin of the Ni–Cu–PGE sulfide ores. Econ. Geol. 100, 439–462.
Lightfoot, P.C., Keays, R.R., Evans-Lamswood, D., Wheeler, R., 2012. S saturation history of Nain Plutonic Suite mafic intrusions: origin of the Voisey's Bay Ni–Cu–Co sulfide deposit, Labrador, Canada. Miner. Deposita 47, 23–50.
Maier, W.D., Barnes, S.J., Chinyepi, G., Barton, J.M., Eglington, B., Setshedi, I., 2008. The composition of magmatic Ni–Cu–(PGE) sulfide deposits in the Tati and Selebi-Phikwe belts of eastern Botswana. Mineral Deposita 43, 37–60.
Mao, J.W., Pirajno, F., Zhang, Z.H., Chai, F.M., Wu, H., Chen, S.P., Chen, L.S., Yang, J.M., Zhang, C.Q., 2008. A review of the Cu–Ni sulfide deposits in the Chinese Tianshan and Altay orogens (Xinjiang Autonomous Region, NW China): Principal characteristics and ore-forming processes. J. Asian Earth Sci. 32 (2–4), 184–203.
Mao, Y.J., Qin, K.Z., Barnes, S.J., Tang, D.M., Xue, S.C., Vaillant, M.L., 2017. Genesis of the Huangshannan high-Ni tenor magmatic sulfide deposit in the eastern Tianshan, Northwest China: constraints from PGE geochemistry and Os–S isotopes. Ore Geol. Rev. 90, 591–606.
Mao, Y.J., Qin, K.Z., Li, C., Tang, D.M., 2015. A modified genetic model for the Huangshandong magmatic sulfide deposit in the central Asian orogenic belt, Xinjiang, western china. Miner. Deposita 50 (1), 65–82.
Mao, Y.J., Qin, K.Z., Li, C., Xue, S.C., Ripley, E.M., 2014. Petrogenesis and ore genesis of the Permian Huangshanxi sulfide ore-bearing mafic-ultramafic intrusion in the Central Asian Orogenic Belt, western China. Lithos 200–201 (1), 111–125.

McDonough, W.F., Sun, S., 1995. The composition of the Earth. Chem. Geol. 120, 223–253.
Naldrett, A.J., 2004. Magmatic Sulfide Deposits: Geology, Geochemistry and Exploration. Springer, Berlin, pp. 728.
Naldrett, A.J., 1997. Key factors in the genesis of Noril'sk, Sudbury, Jinchuan, Voisey's Bay, and other world-class Ni–Cu–PGE deposits: implications for exploration. Aust. J. Earth Sci. 44, 283–315.
Naldrett, A.J., 1999. World-class Ni–Cu–PGE deposits: key factors in their genesis. Miner. Deposita 34, 227–240.
Naldrett, A.J., 2011. Fundamentals of magmatic sulfide deposits. In: In: Li, C., Ripley, E.M. (Eds.), Magmatic Ni–Cu and PGE deposits: geology, geochemistry and genesis: reviews in economic geology, vol. 17. Society of Economic Geologists, Denver, pp. 1–50.
Naldrett, A.J., Asif, M., Kristic, S., 2000. The composition of mineralization of the Voisey's Bay Ni-Cu sulfide deposit, with special reference to platinum group elements. Econ. Geol. 95, 845–865.
Ohmoto, H., 1986. Stable isotope geochemistry of ore deposits. In: In: Valley, J.W., Taylor, H.P., O'Neil, J.R. (Eds.), Stable isotopes in high temperature geological processes. Review in Mineralogy and Geochemistry, vol. 16. pp. 491–559.
Peach, C.L., Mathez, E.A., Keays, R.R., 1990. Sulfide melt-silicate melt distribution coefficients for noble metals and other chalcophile elements as deduced from MORB: implications for partial melting. Geochim. Cosmochim. Acta 54, 3379–3389.
Pina, R., Lunar, R., Ortega, L., Gevilla, F., Alapieti, T., Martinez, C., 2006. Petrology and geochemistry of mafic–ultramafic fragments from the Aguablanca Ni–Cu ore barria, southwest Spain. Economy Geology 101, 865–881.
Pirajno, F., Seltmann, R., Yang, Y., 2011. A review of mineral systems and associated tectonic settings of northern Xinjiang, NW China. Geosci. Front. 02 (2), 157–185.
Qin, K.Z., Su, B.X., Sakyi, P.A., Tang, D.M., Li, X.H., Sun, H., Xiao, Q.H., Liu, P.P., 2011. SIMS zircon U-Pb geochronology and Sr–Nd isotopes of Ni-Cu–bearing mafic–ultramafic intrusions in eastern Tianshan and Beishan in correlation with flood basalts in Tarim Basin (NW China): constraints on a ca. 280-Ma mantle plume. Am. J. Sci. 311, 237–260.
Ren, R., Han, B.F., Xu, Z., Zhou, Y., Liu, B., Zhang, L., Chen, J.F., Su, L., Li, J., Li, X.H., Li, Q.L., 2014. When did the subduction first initiate in the southern Paleo-Asian ocean: new constraints from a Cambrian intra-oceanic arc system in west Junggar, NW China. Earth Planet. Sci. Lett. 388 (3), 222–236.
Ridolfi, F., Renzulli, A., Puerini, M., 2010. Stability and chemical equilibrium of amphibole in calc-alkaline magmas: an overview, new thermobarometric formulations and application to subduction-related volcanoes. Contrib. Miner. Petrol. 160 (1), 45–66.
Ripley, E.M., Taib, N.I., Li, C.S., Moore, C.H., 2007. Chemical and mineralogical heterogeneity in the basal zone of the Partridge River Intrusion: implications for the origin of Cu–Ni sulfide mineralization in the Duluth Complex, midcontinent rift system. Contrib. Miner. Petrol. 154, 35–54.
Robinson, B.W., Kusakabe, M., 1975. Quantitative preparation of sulfur dioxide, for sulfur-34/sulfur-32 analyses, from sulfides by combustion with cuprous oxide. Anal. Chem. 47 (7), 1179–1181.
Rui, Z.Y., Goldfarb, R.J., Qiu, Y.M., Zhou, T.H., Chen, R.Y., Pirajno, F., Yun, G., 2002. Paleozoic-early Mesozoic gold deposits of the Xinjiang Autonomous region, Northwestern China. Miner. Deposita 37, 393–418.
Sappin, A.A., Constantin, M., Clark, T., 2011. Origin of magmatic sulfides in a Proterozoic island arc: an example from the Portneuf-Mauricie Domain, Grenville province. Canada. Mineralium Deposita 46 (3), 211–237.
Sengör, A.M.C., Natal'in, B.A., Burtman, V.S., 1993. Evolution of the Altaid tectonic collage and Paleozoic crustal growth in Eurasia. Nature 364, 209–304.
Song, X.Y., Keays, R.R., Zhou, M.F., Qi, L., Ihlenfeld, C., Xiao, J.F., 2009. Siderophile and chalcophile elemental constraints on the origin of the Jinchuan Ni-Cu-(PGE) sulfide deposit, NW China. Geochimica Et Cosmochimica Acta 73 (2), 404–424.
Song, X.Y., Li, X.R., 2009. Geochemistry of the Kalatongke Ni–Cu–(PGE) sulfide deposit, NW china: implications for the formation of magmatic sulfide mineralization in a post collisional environment. Miner. Deposita 44 (3), 303–327.
Song, X.Y., Xie, W., Deng, Y.F., Crawford, A.J., Zhang, W.Q., Zhou, G.F., Deng, G., Cheng, S.L., Li, J., 2011. Slab break-off and the formation of Permian mafic–ultramafic intrusions in southern margin of Central Asian orogenic belt, Xinjiang, NW China. Lithos 127, 128–143.
Song, X.Y., Yi, J.N., Chen, L.M., She, Y.W., Liu, C.Z., Dang, X.Y., Yang, Q.A., Wu, S.K., 2016. The giant Xiarihamu Ni–Co sulfide deposit in the east Kunlun orogenic belt, northern Tibet plateau, China. Econ. Geol. 111, 29–55.
Su, B.X., Qin, K.Z., Sakyi, P.A., Li, X.H., Yang, Y.H., Sun, H., Tang, D.M., Liu, P.P., Xiao, Q.H., Malaviarachchi, S.P.K., 2011. U-Pb ages and Hf–O isotopes of zircons from Late Paleozoic mafic–ultramafic units in the southern Central Asian Orogenic Belt: tectonic implications and evidence for an Early-Permian mantle plume. Gondwana Res. 20, 516–531.
Sun, T., Qian, Z.Z., Li, C.S., Xia, M.Z., Yang, S.H., 2013. Petrogenesis and economic potential of the Erhongwa mafic–ultramafic intrusion in the Central Asian Orogenic Belt, NW china: constraints from olivine chemistry, U-Pb age and hf isotopes of zircons, and whole-rock Sr–Nd–Pb isotopes. Lithos 182 (7), 185–199.
Tang, D., Qin, K., Li, C., Qi, L., Su, B., Qu, W., 2011. Zircon dating, Hf–Sr–Nd–Os isotopes and PGE geochemistry of the Tianyu sulfide-bearing mafic–ultramafic intrusion in the central Asian orogenic belt, NW China. Lithos 126 (1–2), 84–98.
Tang, D., Qin, K., Su, B., Sakyi, P.A., Mao, Y., Xue, S., 2014. Petrogenesis and mineralization of the Hulu Ni-Cu sulfide deposit in Xinjiang, NW China: constraints from Sr-Nd isotopic and PGE compositions. Int. Geol. Rev. 56 (6), 711–733.
Thompson, A.B., 1992. Water in the earth's upper mantle. Nature 358 (6384), 295–302.
Wang, M., Guo, X., Michalak, P.P., Xia, Q., Xiao, F., Wang, W., 2015. Origin of the Tudun Cu–Ni sulfide deposit in the eastern Tianshan, NW China: constraints on the geochemistry of platinum group elements. Ore Geol. Rev. 64 (1), 445–454.
Wang, R.M., Zhao, C., 1991. Kalatongke Cu–Ni sulfide No.1 ore deposit in Xinjiang. Beijing. Geological Publishing House, pp. 298 (in Chinese with English abstract).
Wang, R.M., Liu, D.Q., Ying, D.T., 1987. Cu–Ni sulfide deposits in the Tudun-Huangshan region, Hami, Xinjiang: Genet controls exploration implications. Miner Rocks 7, 1–152 (in Chinese).
Wei, B., Wang, Y. Christina, Li, C., Sun, Y., 2013. Origin of PGE-depleted Ni-Cu sulfide mineralization in the Triassic Hongqiling No.7 orthopyroxenite intrusion, Central Asian Orogenic Belt, Northeastern China. Economic Geology 108, 1813–1831.
Wood, B.J., Bryndzia, L.T., Johnson, K.E., 1990. Mantle oxidation state and its relationship to tectonic environment and fluid speciation. Science 248 (4953), 337–345.
Woodland, A.B., Koch, M., 2003. Variation in oxygen fugacity with depth in the upper mantle beneath the Kaapvaal craton, southern Africa. Earth Planet. Sci. Lett. 214 (1), 295–310.
Workman, R.K., Hart, S.R., 2005. Major and trace element composition of the depleted MORB Mantle (DMM). Earth Planet. Sci. Lett. 231 (1–2), 53–72.
Xia, M.Z., Jiang, C.Y., Li, C., Xia, Z.D., 2013. Characteristics of a newly discovered Ni–Cu sulfide deposit hosted in the Poyi ultramafic intrusion, Tarim craton, NW China. Econ. Geol. 108, 1865–1878.
Xiao, F., Wang, M.F., Jiang, C.L., Yang, W.S., 2013. Platinum group elements geochemistry and its implication for the Xiangshan Cu–Ni sulfide deposit, east Tianshan, China. Geolog. Sci. Technol. Inf. 32 (1), 125–186 (in Chinese with English abstract).
Xiao, W.J., Windley, B.F., Yuan, C., Sun, M., Han, C.M., Lin, S.F., Chen, H.L., Yan, Q.R., Liu, D.Y., Qin, K.Z., Li, J.L., Sun, S., 2009. Paleozoic multiple subduction-accretion processes of the southern Altaids. Am. J. Sci. 309, 221–270.
Xiao, W.J., Zhang, L.C., Qin, K.Z., Sun, S., Li, J.L., 2004. Paleozoic accretionary and collisional tectonics of the Eastern Tianshan (China): implications for the continental growth of central Asia. Am. J. Sci. 304, 370–395.
Xinjiang Geological Survey, 2014. Work summary of the Lubei Cu–Ni deposit, Shanshan county, Xinjiang. Unpublished report, pp.1–20 (in Chinese).
Tian, J.T., Li, D.H., Wang, J.L., Wang, C., Zhang, X.J., 2017. An investigation report of magmatic Ni–Cu deposit in the Lubei prospect, Shanshan County, Xinjiang. Xinjiang Land and Resources Department, pp. 1–360 (in Chinese).
Yang, W.Z., Ren, Y., Tian, J.T., She, J.Z., Yang, G.G., 2017. The discovery of the Lubei Ni–Cu sulfide ore deposit and its significance for further exploration in east Tianshan, China. Bull. Mineral., Pet. Geochem. 36, 112–120 (in Chinese with English abstract).
Zhang, M., Li, C., Fu, P., Hu, P., Ripley, E.M., 2011. The Permian Huangshanxi Cu–Ni deposit in western China: intrusive–extrusive association, ore genesis, and exploration implications. Miner. Deposita 46 (2), 153–170.
Zhang, Z.W., Tang, Q.Y., Li, C.S., Wang, Y.L., Ripley, E.M., 2017. Sr–Nd–Os–S isotope and PGE geochemistry of the Xiarihamu magmatic sulfide deposit in the Qinghai-Tibet plateau, China. Miner. Deposita 52, 51–68.
Zhao, Y., Xue, C., Zhao, X., Yang, Y.Q., Ke, J., 2015a. Magmatic Cu–Ni sulfide mineralization of the Huangshannan mafic–ultramafic intrusion, eastern Tianshan, China. J. Asian Earth Sci. 105, 155–172.
Zhao, Y., Xue, C., Zhao, X., Yang, Y., Ke, J., Zu, B., 2015b. Variable mineralization processes during the formation of the Permian Hulu Ni-Cu sulfide deposit, Xinjiang, Northwestern China. J. Asian Earth Sci. 126, 1–13.
Zhou, M.F., Lesher, C.M., Yang, Z.X., Li, J.W., Sun, M., 2004. Geochemistry and petrogenesis of 270 Ma Ni–Cu (PGE) sulfide-bearing mafic intrusions in the Huangshan district, Eastern Xinjiang, Northwestern China: implication for the tectonic evolution of the Central Asian Orogenic Belt. Chem. Geol. 209, 233–257.